Ore Geology Reviews 150 (2022) 105169

Contents lists available at ScienceDirect

Ore Geology Reviews

journal homepage: www.elsevier.com/locate/oregeorev

Geochemistry of apatite individuals in Zhijin phosphorites, South China: Insight into the REY sources and diagenetic enrichment

Haiying Yang [a,b], Zhifang Zhao [a,b,c,d,*], Xiaomin Cao [e,*], Haifeng Fan [f], Jiafei Xiao [f], Yong Xia [f], Min Zeng [a,c,d]

[a] School of Earth Sciences, Yunnan University, Kunming 650500, China
[b] Institute of International River and Eco-security, Yunnan University, Kunming 650500, China
[c] Research Center of Domestic High-resolution Satellite Remote Sensing Geological Engineering, University of Yunnan Province, Kunming 650500, China
[d] MNR Key Laboratory of Sanjiang Metallogeny and Resources Exploration & Utilization, Kunming 650051, China
[e] Yunnan Geology Survey, Kunming 650000, China
[f] State Key Laboratory of Ore Deposit Geochemistry, Institute of Geochemistry, Chinese Academy of Sciences, Guiyang 550081, China

ARTICLE INFO

Keywords:
Apatite
Zhijin phosphorite
REY enrichment
Diagenesis
South China

ABSTRACT

Marine sedimentary phosphorites are rich in rare earth elements (REE) and yttrium (REY) which primarily hosted in collophanite composed of closely-packed apatite nanocrystals. Limited by small particle diameters, the fine metallogenic process of apatite crystals and REY enrichment remains unknown. To address this, using early Cambrian REY-rich phosphorite from Zhijin, South China as an example, mineralogical and in situ geochemical characteristics of apatite individuals were analyzed and compared with collophanites. Our study found that: (1) the apatite individuals, with diameters between 40 and 100 μm, were divided into authigenic/diagenetic apatites, terrigenous clastic apatites, and hydrothermally altered apatites; (2) Terrigenous clastic apatites have highest ∑REY levels (4673–12232 ppm) and lowest Y/Ho (23–28), in addition, Y/Ho showed negative relationships with ∑REY in all apatite monominerals, as well as bulk phosphorites; (3) Compared with collophanites and old phosphorite, authigenic/diagenetic apatite individuals showed similar REY patterns, in addition, diagenetic apatites have higher ∑REY, Ce/Ce* and Eu/Eu* ratios but lower $(La/Yb)_N$ and $(La/Sm)_N$ (>0.5) ratios relative to authigenic apatite individuals and collophanites. This dataset indicated that weathering of terrestrial magmatic rocks provided not only clastic apatites but also REY into the South China ocean during the early Cambrian, mixed with REY derived from deep seawater. Authigenic apatite individuals form similarly to apatite nanocrystals in collophanites, with diagenetic modification playing vital role. During this process, apatite individuals grew up and underwent stronger diagenesis than apatite nanocrystals in collophanites, absorbing REY from porewater, which resulted in higher REY concentrations in apatite individuals. This study provides new data and insight into the formation of authigenic/diagenetic apatite individuals and improves our understanding of REY sources and diagenetic effects on REY enrichment.

1. Introduction

Rare earth elements plus Y (REY) are important resources in 21st century, widely used in new technology industries, which include national defense, military, aerospace, clean energy, special materials, and others. Recently, high-tech industries increased the global demand for REY. Most countries have listed REY as a key mineral resource and attached great importance to studying REY mineralization. Typical REY deposits come from carbonate rocks, alkaline rocks/alkaline granite, such as Bayan Obo, Yinachang, and Mianning-Dechang deposits (Ye et al., 2013; Li and Zhou, 2015; Fan H.R. et al., 2016; Liu et al., 2019). Furthermore, supergenetic weathering type/ion adsorption clay-type (Bao and Zhao, 2008; Wang et al., 2018), placer type (Yuan et al., 2012), and sedimentary type (deep-sea mud and phosphorite) (Kato et al., 2011; Emsbo et al., 2015) could provide REY resources. Among them, phosphorite contained enriched levels of middle REEs (MREE) and especially scarce heavy REEs (HREEs) (Emsbo et al., 2015).

Sedimentary phosphorite deposits occur worldwide, especially in Jordan, North America, South China, Australia, and South Africa. Furthermore, phosphorite formed across multiple geological periods,

* Corresponding authors at: School of Earth Sciences, Yunnan University, Kunming 650500, China (Z. Zhao).
E-mail addresses: zhaozhifang@ynu.edu.cn (Z. Zhao), cxyfcy@sina.com (X. Cao).

https://doi.org/10.1016/j.oregeorev.2022.105169
Received 29 May 2022; Received in revised form 9 October 2022; Accepted 24 October 2022
Available online 28 October 2022

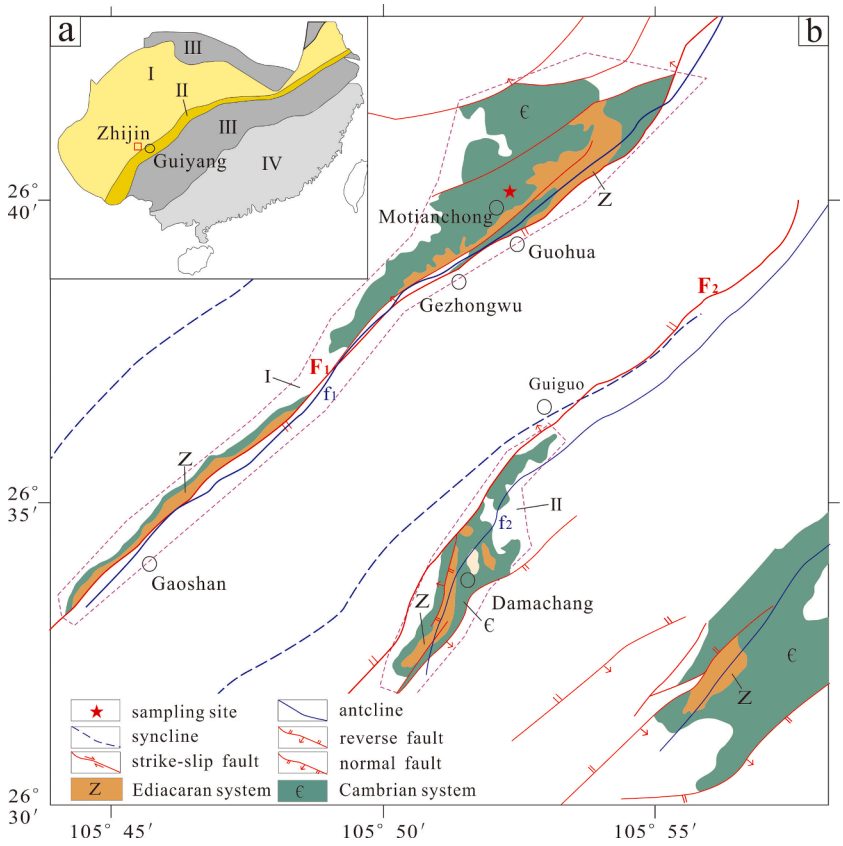

Fig. 1. (a) Simplified paleogeographic map of the Yangtze Platform in the early Cambrian, modified after Steiner et al. (2001). (b) Geological map of the Zhijin area.

including the Neoproterozoic, Cambrian, Carboniferous, Jurassic, Cretaceous, Tertiary, and modern sediments. Among them, REY-enriched phosphorites formed primarily during the Paleozoic Era (Emsbo et al., 2015). For example, REY concentrations (∑REY) in Upper Devonian phosphorite reach levels as high as 18000 ppm (Kato et al., 2011; Emsbo et al., 2015), higher than ion adsorption in South China (Bao and Zhao, 2008; Wang et al., 2018). Therefore, phosphorite could serve as a new REY resource and probably meet global REY demands (Kato et al., 2011; Emsbo et al., 2015).

REY mineralization and occurrence have attracted significant research attention recently. Several viewpoints have been proposed to explain REY enrichment in sedimentary phosphorite, including: (1) An upwelling paleogeographic area favors REY enrichment. On one hand, seawater and terrigenous inputs supplied sufficient sources of P and REY (Föllmi et al., 2009; Planavsky et al., 2010; Pufahl and Groat, 2017; Yang et al., 2021a), on the other hand, shallow seawater was hydrodynamically fluctuant and facilitated phosphate precipitation and REY enrichment (Chen et al., 2013; Pufahl and Groat, 2017); (2) The paleoenvironment controlled REY enrichment. It has been approed that phosphorite formation was controlled by redox conditions through “Fe redox pumping” (Canfield et al., 2007; Nelson et al., 2010). Meanwhile, Fe- and Mn- oxides preferentially adsorbed MREEs, and REY entered apatite crystals in the pore water during diagenesis (Paul et al., 2019; Yang et al., 2021b). Furthermore, temperature, sedimentary rate, and REY composition in seawater may have played a role in REY enrichment in some degree (Al-Bassam and Magna, 2018; Yang et al., 2021b); (3) Biological activities benefitted REY enrichment. Research showed that biological absorption and organic mineralization controlled the REY cycle in the seawater and pore water, in which organic materials are enriched in MREEs (Henderson, 1984; Freslon et al., 2014). REY-enriched phosphorite always contained enriched MREEs (Emsbo et al., 2015), which implied a biological contribution (Yang et al., 2021b). Furthermore, low Zn isotopic compositions and Cd isotopes similar to modern seawater in phosphorite implied a stronger biological contribution (Fan et al., 2018; Frei et al., 2021); (4) Fe-redox pumping control not only the phosphorite formation in non-upwelling area, but also the REY enrichment of deep sea muds in the Pacific Ocean (Nelson et al., 2010; Kashiwabara et al., 2018). These processes happened along with the Fe oxide precipitation in oxic conditions and Fe dissolution and release under redox interface; (5) Diagenesis was the key factor in REY enrichment. Most recent phosphorite exhibit seawater-like REE patterns, while deviations from modern seawater REE patterns could be ascribed to diagenetic alteration (McArthur and Walsh, 1984; Shields and Stille, 2001). Reynard et al. (1999) proposed a comparison of $(La/Yb)_N$ vs $(La/Sm)_N$ to identify diagenetic stages, previous reports regarding Ediacaran-early Cambrian phosphorite, Permian conodont, Jurassic fish bone, and Cenozoic phosphorite suggested that REY entered apatites during early diagenesis (Lumiste et al., 2019; Yang et al., 2021b; Yang et al., 2022). Geologists found that different mechanisms affect REY enrichment differently at the macro level, but the specific roles of different metallogenic mechanisms in REY enrichment remain unclear. Furthermore, there is no consensus on the control mechanism of REY enrichment.

Phosphate minerals, previously termed collophanite, were composed of apatite nanocrystals (Liu, 2008; Liu and Zhou, 2017; Liao et al., 2019; Zhang et al., 2019; Yang et al., 2021b). Research showed that REY occurred mainly in apatite by isomorphic substitution (Huang et al., 2021; Zhang et al., 2021), while small amounts of REY were adsorbed by phosphate or clay minerals (Zhang et al., 2007) and existed as REE independent minerals (Liu, 2008). Hence, the formation of phosphate minerals recorded key information of REY enrichment. Phosphate minerals in sedimentary phosphorite include carbon-free fluorapatite (fluorapatite) and a small amount of carbonate-fluorapatite (francolite) that comprise closely-packed, nm to μm-scale crystals (Liu and Zhou, 2017; Liao et al., 2019; Yang et al., 2021b). Conducting a detailed study about phosphate minerals is expected to provide further evidence for

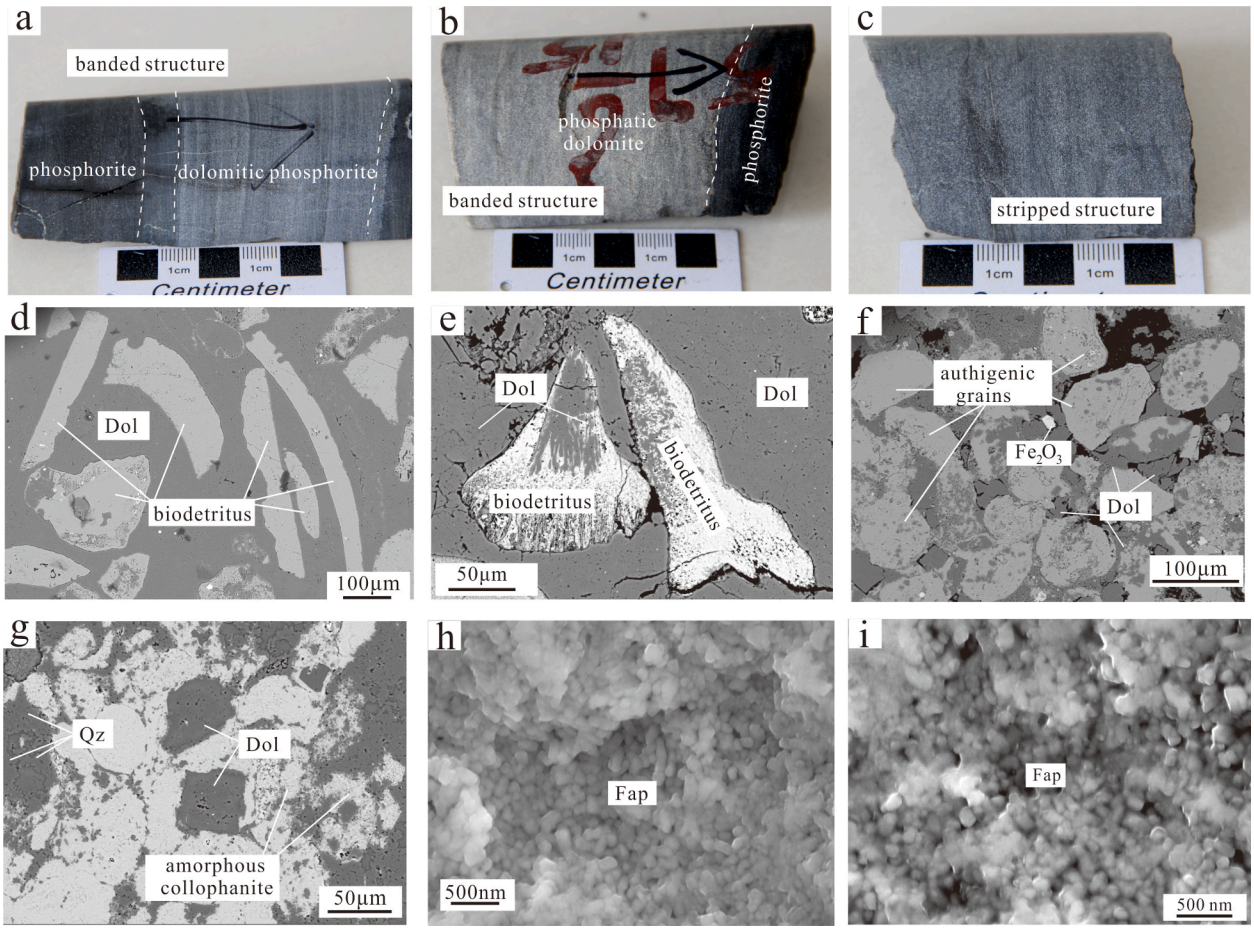

Fig. 2. The characteristics of hand specimens (a)-(c) and phosphate minerals (d)-(i) from the Gezhongwu Formation, early Cambrian in Zhijin phosphorite, South China. Figures (d)-(i) are backscattered electron images, collected with the signal acquisition conditions of a 20 kV voltage and a 100 nA current. (a), (b) banded phosphorite; (c) stripped phosphorite; all francolite grains were divided into (d, e) biodetritus, (g) authigenic grains, and (h) amorphous collophanite; these francolite grains were composed of tightly packed apatite nanocrystals (f, i), with six-party and granular textures and nanoscale diameters. Among the pictures, f and i are from Yang et al. (2021b). Abbreviations: Dol = dolomite; Qz = quartz; Fap = francolite.

phosphorite formation and REY enrichment. However, limited by the small diameter of apatite nano-crystals, fine mineralogic and geochemiscal characteristics were difficult to obtain, severely restricting the understanding of apatite formation and REY enrichment.

The early Cambrian era was an important phosphorus-forming period (Cook, 1992), which occurred coevally with localized REY-rich phosphorite in Zhijin, South China. The Zhijin phosphorite has been studied extensively for its sedimentary, petrographic, and geochemical characteristics (Zhang et al., 2003; Liu, 2008; Chen et al., 2010), and many fine mineralogical studies were conducted in recent years (Liu et al., 2020; Yang et al., 2021b; Zhang et al., 2021; He et al., 2022; Yang et al., 2022). Previous studies provided significant information, which allows Zhijin to serve as an ideal objective for analyzing microscale apatite formation and REY enrichment.

In this study, Zhijin phosphorite was examined, fine-scale mineralogical and geochemical characteristics of nano-scale apatite aggregations (collophanite) and apatite individuals were analyzed using scanning electron microscopy (SEM), electron microprobe analysis (EMPA), and laser ablation inductively coupled plasma mass spectrometry (LA-ICP-MS). The aim was to classify apatite individuals in Zhijin phosphorite, to trace the sources of apatites and REY, and to reveal the authigenic apatite formation and REY enrichment mechanism. This work provides a further understanding of REY sources and enrichment mechanism in marine sedimetary phosphorite.

2. Geological setting

2.1. Paleogeography

South China underwent multiple tectonic activities after Jinningian tectonics (900–820 Ma), during which the Yangtze Block and Cathaysia Block aggregated and the Jiangnan Orogenic Belt formed (Shu, 2012; Zhang et al., 2013). Thereafter, the ancient South China Plate rapidly underwent rifting and glaciation with relatively stable tectonic movements (Shu, 2012). Along with the supercontinent fragmentation of Rodinia during the late Neoproterozoic, the Yangtze Block and Cathaysia Block began to break up (Wang and Li, 2003), which caused the paleographic framework of deepening water from the NW shelf towards the SE ocean basin (Liu et al., 1993; Zhang et al., 2013). In the early Cambrian, the South China Plate underwent steadier supercontinent break-ups but maintained the same paleographic framework of the late Neoproterozoic (Liu et al., 1993).

The early Cambrian was an important lithofacies-paleogeographic development stage in South China. During this period, the facies regions in South China were composed of shallow-water carbonate platform facies (Fig. 1a I), transitional facies (Fig. 1a II), and deep-water slope and basin facies (Fig. 1a III) from the northwest to southeast (Steiner et al., 2001). Plenty of phosphorites formed in the carbonate platforms during the early Cambrian such as Kunyang in Yunnan, Zhijin in Guizhou, and Hanyuan in Sichuan (Ye et al., 1989). Among them, Zhijin phosphorite deposit formed in the early Cambrian phase,

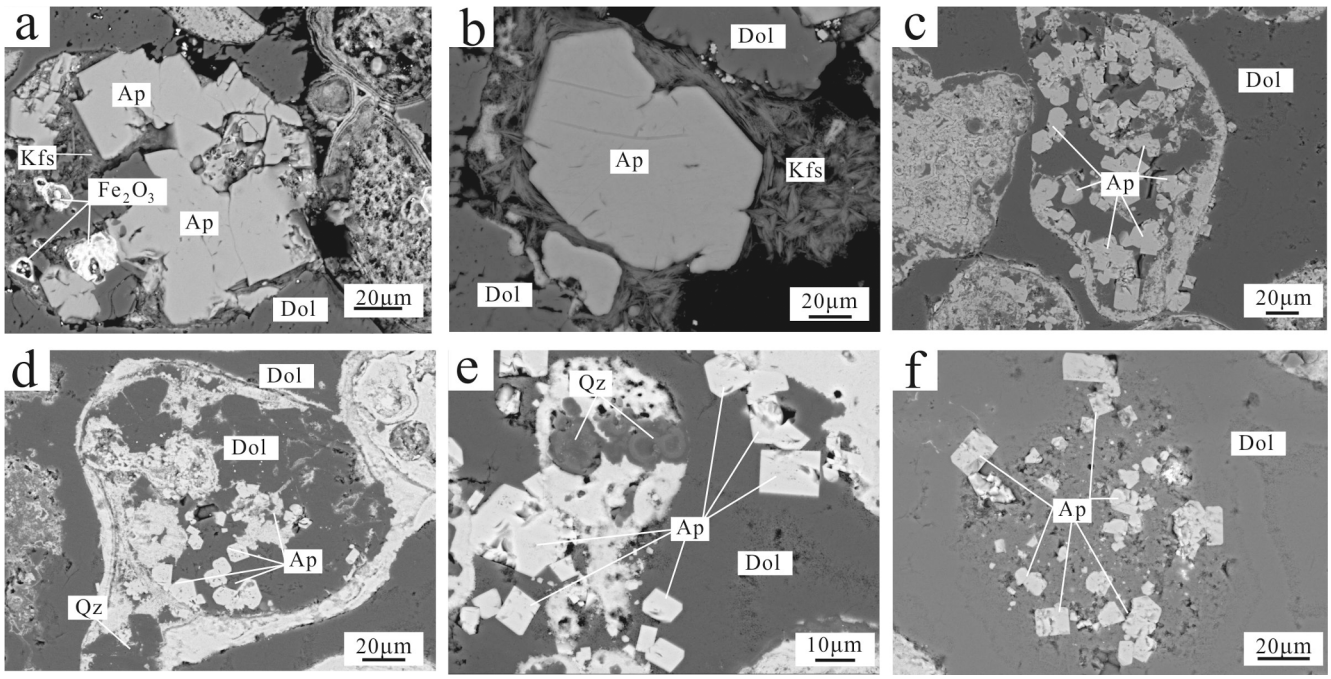

Fig. 3. Symbiotic relationship between apatite individuals with other ore minerals. Figures are collected under conditions similar with Fig. 2. (a, b) apatite individuals with larger diameters piled up with K- feldspar; (c, d) apatite individuals hosted in biodetritus; (e, f) apatite individuals distributed dispersedly and were cemented by dolomite. Abbreviations: Ap = apatite; Dol = dolomite; Qz = quartz; Kfs = K- feldspar.

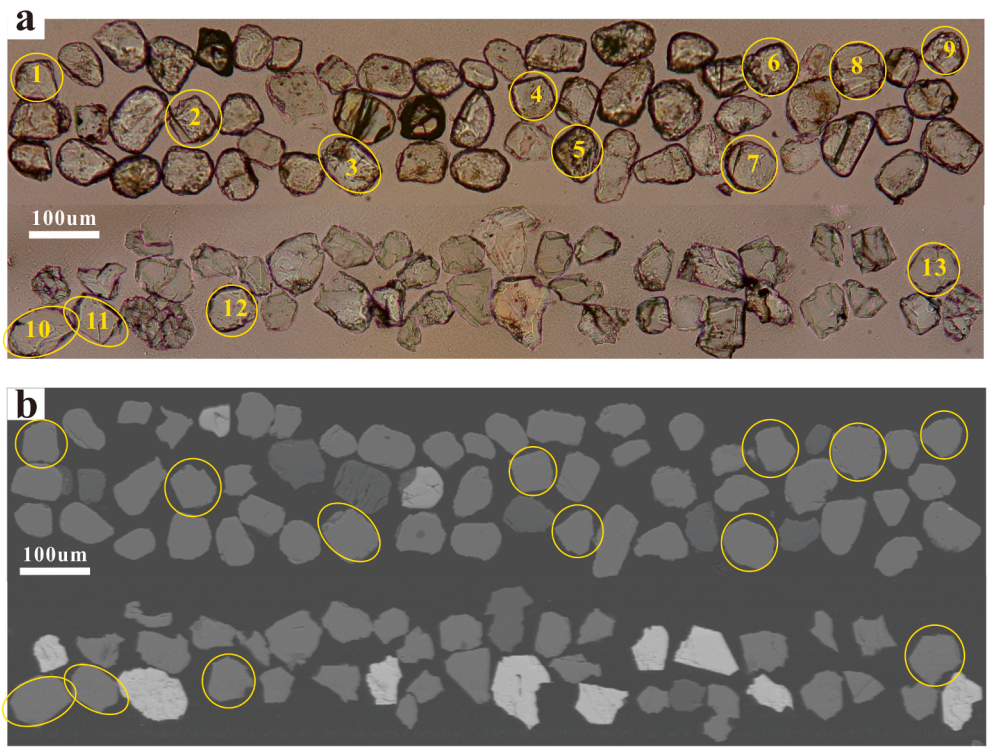

Fig. 4. Characteristics of apatite individuals under transmitted, plane-polarized light (a) and a scanning electron microscope (b). Corresponding backscattered electron image under SEM with a 10-kV, 4.5-nA beam. All apatite individuals were selected individually. Circled numbers represent in situ analysis points, consistent with the serial numbers in Tables 2 and 3.

containing enriched REY and showing great potential REY resources. Early isotope dating suggested early Cambrian phosphorite in South China formed in 587 ± 17 Ma (Cowie and Johnson, 1985), 562 ± 5.7 Ma (Yang et al., 1996) by Rb-Sr and Sm-Nd isotopes, respectively. Shi (2005) subsequently conducted Sm-Nd/Rb-Sr isotopes and suggested that Zhijin phosphorite started formation in 541 ± 12 Ma. Reported re-Os isochron age of the sulfide ore layer in Niutitang Formation were confirmed to 537 ± 10 Ma (Jiang et al., 2004) and 521 ± 5 Ma (Xu et al., 2011). Hence, Zhijin early Cambrian phosphorite were deemed to form during ~ 541–521 Ma.

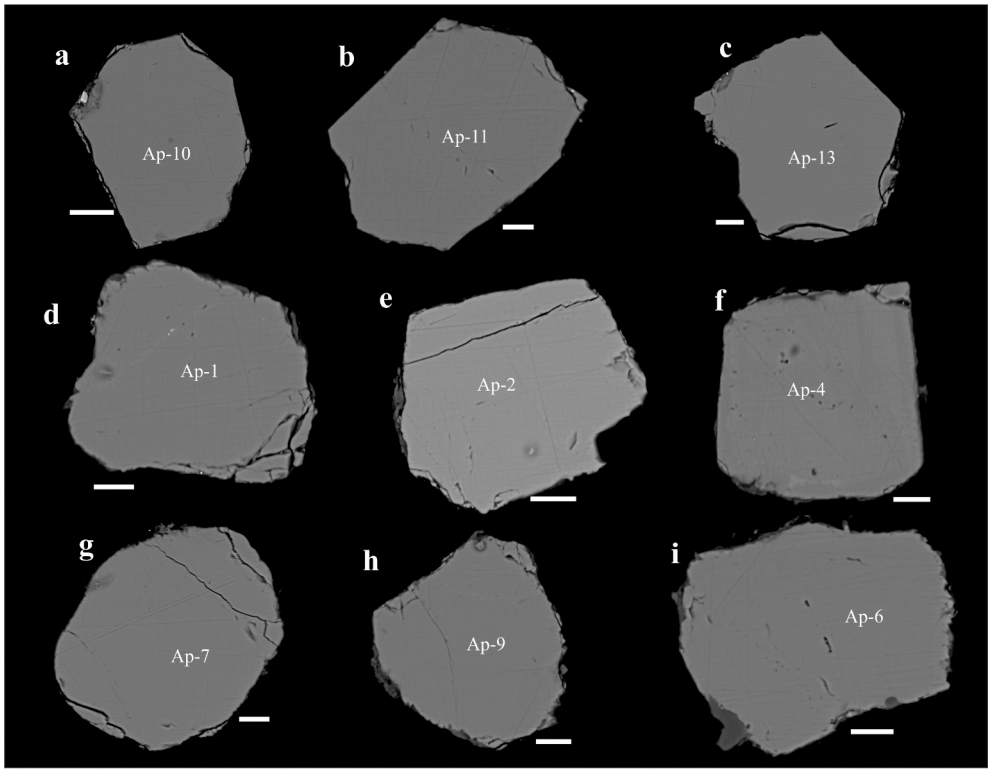

Fig. 5. Characteristics of mineralogical textures of individual apatites from the early Cambrian Zhijin phosphorite, South China. (a-c) six-party texture; (d-f) cube-like texture; (g-h) granular texture; (i) irregular texture. All images were collected via SEM, each scale bar represents 20 μm.

Table 1
Major and trace element compositions of apatite individuals from Zhijin deposit, the Central Guizhou, South China.

Numbers	Li	Na_2O	Al_2O_3	SiO_2	P_2O_5	K_2O	CaO	V	Cr	FeO	Sr	Ba	Pb	Th	U
AP-1	1.92	0.06	0.05	0.27	41.47	0.01	57.51	5.43	0.14	0.27	401.91	7.19	3.87	5.73	4.46
AP-2	0.09	0.02	0.04	0.26	39.75	0.01	59.58	8.19	0.00	0.03	412.36	0.58	4.27	15.15	29.00
AP-3	0.21	0.01	0.00	0.42	39.55	0.00	59.13	13.39	0.67	0.03	496.68	0.95	5.37	208.21	92.13
AP-4	1.36	0.03	0.05	0.34	39.89	0.03	58.97	8.45	0.31	0.10	316.08	3.89	3.20	28.61	7.49
AP-5	5.18	0.02	0.19	0.71	39.38	0.07	58.77	4.25	0.00	0.20	328.89	5.11	3.69	14.32	3.51
AP-6	2.59	0.10	0.19	0.33	39.87	0.06	58.64	2.42	1.44	0.25	147.11	4.84	3.15	2.47	12.83
AP-7	3.24	0.07	0.00	0.19	39.89	0.00	58.57	6.46	0.14	0.60	360.12	6.90	4.51	13.55	7.57
AP-8	7.59	0.13	0.17	0.63	39.45	0.06	58.30	36.83	0.00	0.10	287.02	7.09	3.95	16.63	3.33
AP-9	0.37	0.08	0.00	0.42	38.99	0.00	58.93	9.94	0.22	0.05	529.54	1.08	5.46	101.30	33.85
AP-10	0.00	0.01	0.00	0.03	40.09	0.00	59.43	0.07	0.43	0.01	2444.05	0.53	1.71	0.00	2.52
AP-11	0.00	0.02	0.00	0.01	40.60	0.00	58.82	0.02	0.40	0.01	2319.59	1.31	6.22	0.21	8.48
AP-12	0.03	0.02	0.00	0.00	40.49	0.00	58.98	0.10	0.00	0.01	1765.18	0.78	0.89	0.05	6.22
AP-13	0.03	0.03	0.00	0.14	40.24	0.00	58.96	0.06	0.76	0.01	2106.27	0.90	9.33	0.03	20.06
Mean	**1.74**	**0.05**	**0.05**	**0.29**	**39.97**	**0.02**	**58.81**	**7.35**	**0.35**	**0.13**	**916.52**	**3.17**	**4.28**	**31.25**	**17.80**
δ	**2.38**	**0.04**	**0.08**	**0.22**	**0.63**	**0.03**	**0.52**	**9.85**	**0.41**	**0.17**	**879.70**	**2.74**	**2.10**	**59.63**	**24.49**

Note: Units for Li, Na_2O, Na_2O, Al_2O_3, SiO_2, SiO_2, K_2O, and CaO are wt.%, while for other elements are ppm. Mean represents arithmetic mean value, δ represents standard deviation. The following tables also apply.

2.2. Ore deposit geology

2.2.1. Ore bodies

The Zhijin deposits are stratabound and spread northeast along with cores of the Guohua-Gezhongwu Fault/Anticline (F_1/f_1) and Guiguo-Damachang Fault/Anticline (F_2/f_2) (Fig. 1b). The deposits comprise an area of 333 km^2 and are divided into the Xinhua Mining District (I) on the northwestern side and the Damachang Mining District (II) on the southeastern side. The Xinhua Mining District includes the Daga, Motianchong, Guohua, Ganjiayakou, Gezhongwu, and Gaoshan ore blocks, which provide the most phosphate in the Zhijin deposit. The Zhijin deposit had phosphate mineral resources about 3.39 billion tons and potential REY resources (RE_2O_3) of nearly 3.503 million tons, with P2O5 and RE_2O_3 grades of 17.20 g/t and 0.1036 g/t, respectively (Yang et al., 2021a).

Zhijin phosphorites are hosted in the Gezhongwu Formation, occurred in platform carbonate rocks and underlain by Dengying dolomite and overlain by Niutitang sandy shale. The Gezhongwu Formation is usually divided into the lower Gezhongwu Member and upper Gezhongwu Member, comprising dolomitic phosphorite sand striped siliceous phosphorite, respectively (Yang et al., 2021a). Biological fossils are abundant in the Zhijin deposit and include small shell fossils (SSF), macroscopic bacterial colonies, arthropods, sponges, and zooplankton (Wu et al., 1999).

2.2.2. Mineralogy

The texture of Zhijin phosphorites helps classify them into massive, banded, stripped, earthy, and densely massive (detailed descriptions are

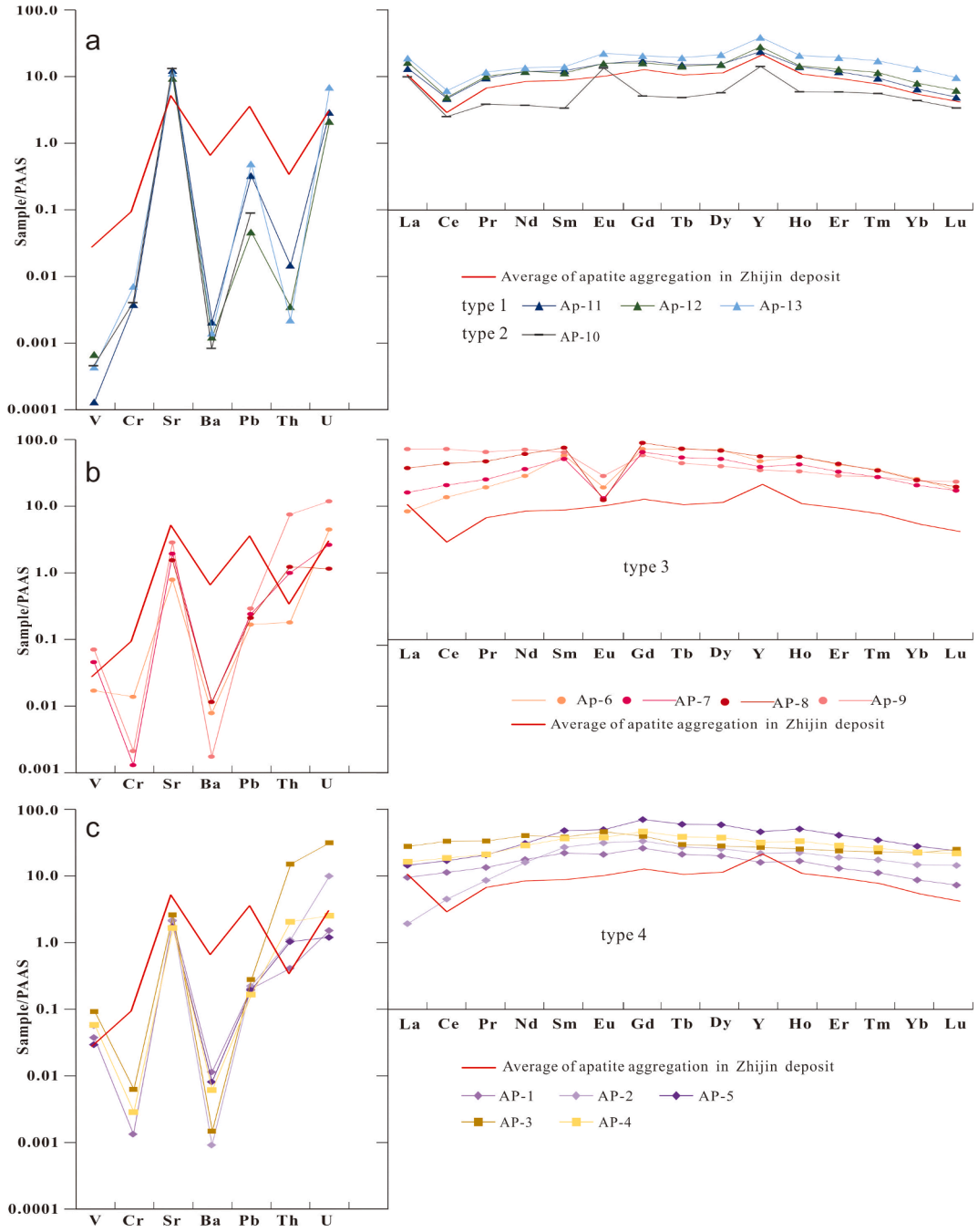

Fig. 6. PAAS-normalized rare earth element distributions of collophanite and apatite individuals with four REY types from Zhijin early Cambrian phosphorite, South China. The collophanite data came from our previous studies (Yang et al., 2021b; He et al., 2022; Yang et al., 2022), with maximum, minimum, and average value distributions. PAAS data are from Taylor and McLennan (1985).

given in Yang et al. (2021b) and Yang et al. (2022)). Among them, banded (Fig. 2a, b) and stripped (Fig. 2c) textures were widespread and typical. Minerals comprised primarily phosphates and gangue minerals including dolomite, calcite, quartz, magnetite, pyrite, K-feldspar, and muscovite. The phosphates were divided into biodetritus (Fig. 2d, e), authigenic grains (Fig. 2f), and amorphous collophanite (Fig. 2g), all were aggregations of apatite nanocrystals. Biodetritus have irregular textures and diameters ranging from 100 to 300 μm and were directionally distributed, composed of hexagonal short-column fluorapatite nanocrystals (Fig. 2h). Authigenic phosphate grains have average diameters of 200–300 μm and were characterized by elliptical, round, and spindly structures, with quartz and dolomite inclusions (Fig. 2f). Generally, authigenic grains and amorphous collophanite both are composed of tightly packed apatite with spherulitic shapes and 20–50 nm in diameter (Fig. 2 i). We have recently reported detailed description about apatite mineral characteristics (Yang et al., 2021b; Yang et al., 2022).

3. Sampling and methodologies

The phosphorite samples were sampled from the Motianchong ore block in the Xinhua Mine District (Fig. 1b). The phosphorite samples were made into polished sections with thicknesses of 30 μm for petrographic analysis, and in situ geochemical results are cited by Yang et al. (2021b) and Yang et al. (2022). Partial phosphorite samples were sieved using different diameters to select apatite individuals. Appropriate

Table 2
Rare earth element compositions of apatite individuals from Zhijin deposit, the Central Guizhou, South China (ppm).

N	La	Ce	Pr	Nd	Sm	Eu	Gd	Tb	Dy	Ho	Er	Tm	Yb	Lu	Y	∑REY	Ce/Ce*	Eu/Eu*	Y/Ho	La/Sm	La/Yb
AP-1	339.51	848.76	111.97	528.81	115.95	14.00	114.83	15.25	82.17	15.72	35.45	4.20	22.91	2.95	404.54	2657.04	0.99	0.87	25.73	0.43	1.09
AP-2	69.31	338.56	72.00	480.61	141.60	32.29	146.67	19.67	105.45	20.99	51.57	6.53	38.51	5.81	551.74	2081.32	0.85	1.04	26.29	0.07	0.13
AP-3	996.59	2510.76	280.61	1216.05	202.12	47.62	174.97	21.54	117.04	24.01	65.10	8.70	58.60	10.16	682.55	6416.40	1.09	1.18	28.42	0.73	1.25
AP-4	587.62	1406.59	176.83	866.06	193.35	39.27	205.71	28.07	156.13	31.34	78.17	9.85	59.89	8.89	808.02	4655.79	1.00	0.91	25.78	0.45	0.72
AP-5	515.83	1269.61	172.72	921.76	250.55	50.99	308.01	42.74	240.60	47.21	110.66	12.90	73.32	9.57	1159.78	5186.24	0.96	0.84	24.57	0.30	0.52
AP-6	294.15	1005.11	157.03	839.28	295.50	19.33	309.94	50.74	281.76	50.50	111.86	12.91	65.77	6.91	1172.11	4672.89	0.99	0.30	23.21	0.15	0.33
AP-7	561.75	1522.31	206.43	1060.15	262.41	13.31	278.99	37.90	206.87	38.85	87.69	10.06	53.02	6.79	964.11	5310.62	1.00	0.23	24.82	0.32	0.78
AP-8	1300.32	3204.36	383.91	1781.36	386.64	12.53	382.75	51.60	274.27	50.43	115.11	12.58	63.54	7.73	1382.40	9409.54	1.04	0.15	27.41	0.50	1.51
AP-9	2499.60	5282.67	530.73	2068.16	329.29	28.67	250.76	31.23	160.90	30.63	76.37	10.07	62.35	9.23	861.62	12232.27	1.05	0.46	28.13	1.12	2.95
AP-10	349.13	187.37	31.84	110.74	17.57	13.64	22.26	3.46	23.42	5.48	15.84	2.07	11.40	1.35	353.99	1149.57	0.37	3.15	64.57	2.93	2.26
AP-11	468.86	352.48	79.51	356.05	64.48	16.07	76.04	10.79	63.11	13.14	32.03	3.55	17.08	1.98	597.39	2152.56	0.41	1.06	45.45	1.07	2.02
AP-12	578.79	366.53	84.11	357.08	59.33	16.24	70.56	10.35	62.35	13.53	34.99	4.30	20.90	2.51	704.45	2385.99	0.37	1.15	52.06	1.44	2.04
AP-13	673.01	462.35	97.33	405.43	73.58	22.92	90.35	13.83	87.63	19.37	52.25	6.43	34.21	3.89	977.82	3020.40	0.40	1.29	50.47	1.35	1.45
Mean	**710.34**	**1442.88**	**183.46**	**845.50**	**184.03**	**25.14**	**187.06**	**25.94**	**143.21**	**27.79**	**66.70**	**8.01**	**44.73**	**5.98**	**816.96**	**4717.74**	**0.81**	**0.97**	**34.38**	**0.83**	**1.31**
δ	**621.53**	**1462.71**	**141.49**	**577.75**	**116.10**	**13.52**	**111.91**	**15.89**	**84.96**	**15.11**	**33.16**	**3.76**	**21.38**	**3.12**	**309.12**	**3173.42**	**0.30**	**0.76**	**13.71**	**0.77**	**0.83**

Note: $Ce/Ce^* = 2Ce_N/(La_N + Nd_N)$, $Eu/Eu^* = 2Eu_N/(Sm_N + Gd_N)$ (Bau and Dulski, 1996).

apatite individuals were pasted into an orderly resin target for petrographic and in situ geochemical analyses.

3.1. Petrographic analyses of apatite individuals

The petrographic characteristics were analyzed via a JSM-7800F field emission scanning electron microscope (SEM) (Jeol Ltd., Japan) at the State Key Laboratory of Ore Deposit Geochemistry at the Institute of Geochemistry, Chinese Academy of Sciences. The sections and targets were sprayed with carbon, which made the section conductive, then placed in the SEM. The backscattered electron images were collected with a 10-kV, 4.5-nA beam, while EDS was conducted using a 10-kV, 4.5-nA beam.

3.2. In situ elemental analyses of apatite individuals

In situ trace elements of apatite, and individuals were analyzed at the State Key Laboratory of Ore Deposit Geochemistry at the Institute of Geochemistry, Chinese Academy of Sciences. The samples were ablated using a 44–60 μm laser beam and mixed with an H_2/He carrier gas; that aerosol was sent into the ICP-MS for elemental signal collection. Every cyclicality of signal collection included a 30 s blank and a 50 s sample ablated signal. All elemental abundances were calibrated using NIST612 and NIST610 materials issued by the National Institute Standard Technology (NIST), using DUR as apatite and MACS as carbonate external standards. The reference levels for the external standards are available online at https://georem.mpch-mainz.gwdg.de/. Internal corrections were applied using elemental abundances of Ca determined using EPMA analyses to correct matrix effects between the standards and the analyzed minerals. The detection limit was at the ppb level. The signal was dealt with ICPMSDataCal (Liu et al., 2008) using multiple external standards–signal internal standard methods (Chew et al., 2016). Ce and Eu anomalies were calculated according to the following equation: $Ce/Ce^* = 2Ce_N/(La_N + Nd_N)$, $Eu/Eu^* = 2Eu_N/(Sm_N + Gd_N)$ (Bau and Dulski, 1996).

4. Analysis results

4.1. Petrographic characteristics of apatites

We have found that phosphate minerals are mainly existed in the form of fluorapatite nanocrystals constituting biodetritus, authigenic grains, and amorphous collophanite (Fig. 2d-i). Most collophanites, including biodetritus, containing various dolomite, quartz, and clay mineral, causing untight surface and microgranular textures (Fig. 2 d-g). Besides this, we now discovered apatite individuals with larger diameters, all apatite individuals have clean and dense transection (Fig. 3), dislike those of biodetritus. Three kinds of symbiotic relationship between these apatite individuals with other ore minerals were recognized: (1) apatites with allotriomorphic texture and diameter around 80–100 μm were piled up with K- feldspar (Fig. 3a, b); (2) apatites with six-party textures and diameter about 10–30 μm occurred intensively in authigenic grains (Fig. 3c) or were hosted in biodetritus (Fig. 3d); (3) apatites having cubic textures and diameter in 10–20 μm distributed dispersedly among and were cemented by dolomite (Fig. 3e, f). Both kinds (2) and (3) have idiomorphic textures and were symbiosis with and cemented by dolomite.

For apatite individuals distributed dispersedly, in this study, we selected apatite individuals with diameters much larger ranging from 40 to 100 μm for petrographic and geochemical observation. The surfaces of all apatite individuals were smooth and dense (Fig. 4). Their textures were divided into: six-party texture (Fig. 5a-c) including Ap-10 to Ap-13; cube-like texture (Fig. 5d-f) including Ap-1 to Ap-5; granular texture (Fig. 5g) including Ap-7 to Ap-9; and irregular texture (Fig. 5h, i), such as Ap- 6.

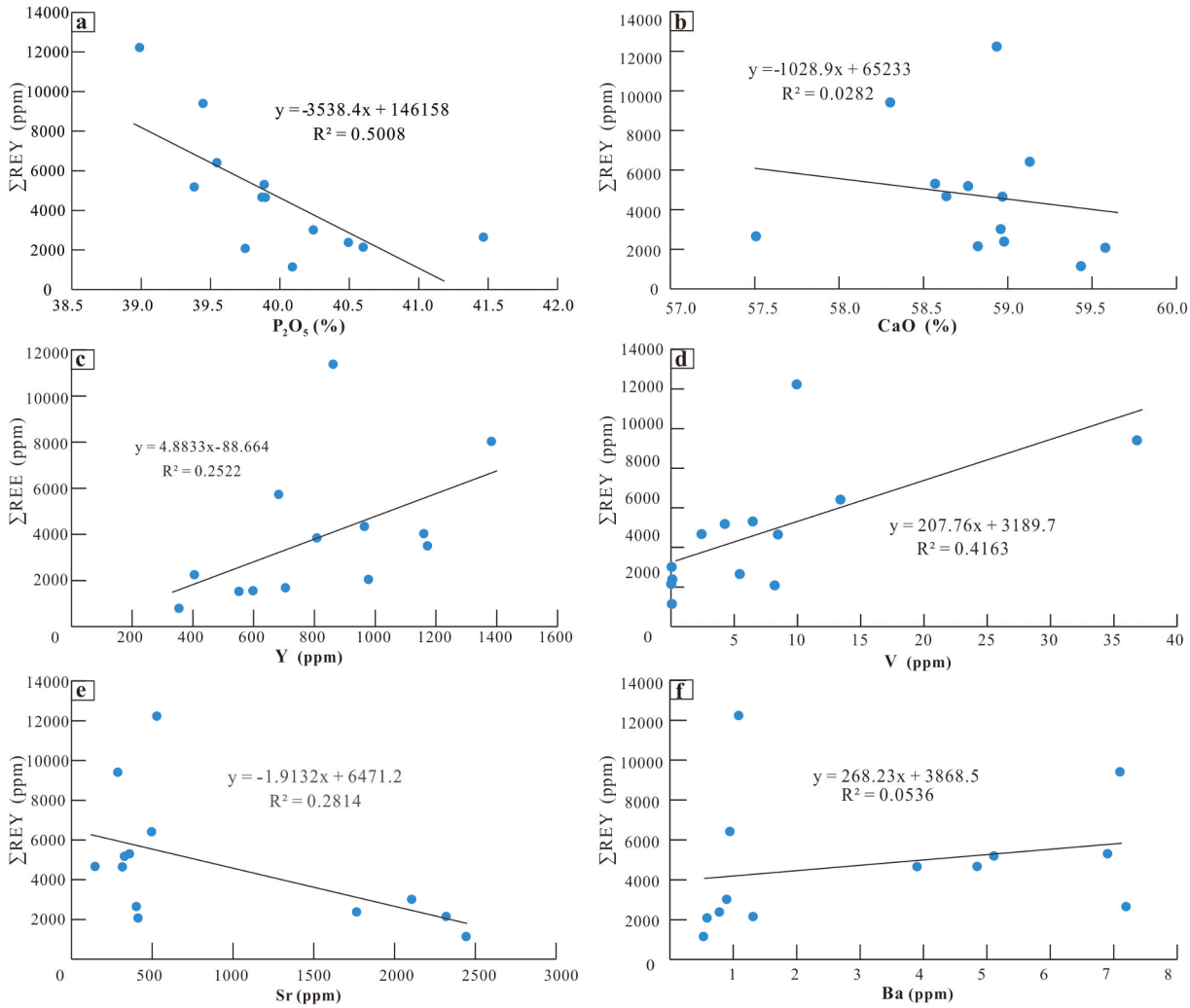

Fig. 7. Relationships between ∑REY and P_2O_5(a), CaO (b), Y (c), V (d), Sr (e), and Ba (f) of apatite individuals from Zhijin phosphorite.

4.2. *Chemical compositions of apatite individuals*

In situ major and trace elements of early Cambrian apatite individuals were listed in Table 1. The apatite individuals have P_2O_5 levels that range from 38.99 to 41.47 % with small variability (mean = 39.97 %, standard deviation (δ) = 0.63), and CaO levels of 57.51–59.58 % (mean = 58.81 and $\delta = 0.52$). The data show that mean values of V, Cr, FeO, Sr, Ba, Pb, Th, and U were 7.35 ppm ($\delta = 9.85$), 0.35 ppm ($\delta = 0.41$), 0.13 ppm ($\delta = 0.17$), 916.52 ppm ($\delta = 879.70$), 3.17 ppm ($\delta = 2.74$), 4.28 ppm ($\delta = 2.10$), 31.25 ppm ($\delta = 59.63$), and 17.80 ppm ($\delta = 24.49$), respectively. Apatites with six-party apatite individuals (Ap-10 to Ap-13) have higher P_2O_5 (40.09–40.60 %) and Sr (1765.18–2444.05 ppm) concentrations but lower Li, Si, V, Ba, Pb, Th, and U concentrations than other apatite individuals (Fig. 6a).

In situ REY compositions of early Cambrian apatite individuals are listed in Table 2. The ∑REY of apatite individuals ranged from 1149.57 to 12232.27 ppm (mean = 4717.74), with great variability ($\delta = 3172.42$). The Post-Archean Australian Shale (PAAS) normalized REY patterns were divided into the following four groups (Fig. 6): **(1)** MREE-rich REY patterns, found in authigenic six-party apatite individuals (Ap-11 to Ap-13), characterized by weak enrichment of MREE compared to LREEs and HREEs and higher Y/Ho ratios (45.45–52.06), evident La and Y positive anomalies, and remarkably negative Ce anomalies (Fig. 6a); **(2)** There was one apatite individual (Ap-10) that showed MREE-rich patterns along with an obvious positive Eu anomaly, a high Y/Ho ratio (64.57), and low ∑REY (1149.57 ppm) (Fig. 6a); **(3)** right-inclined to MREE enrichment patterns characterized by clear depletion of HREE and weak to remarkable LREE depletions; these apatite individuals (Ap-6, 7, 8, and 9) have notably negative Eu anomalies, low Y/Ho ratios (23.21–28.13), and high ∑REY (4672.89–12232.27 ppm) (Fig. 6b); **(4)** "bell-shaped" to flat REY patterns (found in Ap-1, 2, and 5; Ap-3 and 4, respectively) characterized by weak MREE enrichment as compared to LREEs and HREEs, with low Y/Ho ratios of 24.57–28.42 and ∑REY of 2081.32–6416.40 ppm (Fig. 6c). Compared with a collophanite, apatite individuals have higher and more variable ∑REY. Among the REY patterns, type 1 have similar REY compositions with collophanite (Fig. 6a) (Yang et al., 2021b; He et al., 2022; Yang et al., 2022). Cerium and Eu anomalies differed significantly in different textures of apatite individuals (Table 2). Authigenic six-party apatite individuals have negative Ce anomalies, with Ce/Ce* ratios ranging from 0.37 to 0.41. In contrast, other apatite individuals have no Ce/Ce* ratio anomalies (0.85 to 1.09). The Eu/Eu* ratios of all apatite individuals varied from 0.15 to 3.15, with authigenic six-party apatite individuals having a mean Eu/Eu* of 1.17 (1.06–1.29) and irregular apatite individuals having negative Eu/Eu* of 0.15–0,46. The correlations between ∑REY and other elements showed that ∑REY negatively correlated with P_2O_5 and Sr (Fig. 7a, b), positively correlated with Y and V (Fig. 7c, d), and did not correlate with Ca and Ba (Fig. 7e, f). This differed significantly from apatite aggregations we previously reported; therein, ∑REY showed positive correlations with Y, weakly positive correlations with Sr and Ba, and no correlations with P_2O_5, Fe, SiO_2, or Na_2O (Yang et al., 2021a).

Table 3
Trace element compositions of apatite aggregations in early Cambrian phosphorite from Zhijin deposit, the Central Guizhou, South China (ppm).

Values	V	Cr	Ni	Cu	Zn	As	Rb	Sr	Zr	Ba	Pb	Th	U	La	Ce	Pr	Nd
Mean	**4.32**	**10.61**	**1.63**	**7.15**	**186.86**	**12.42**	**7.46**	**1054.38**	**5.15**	**438.97**	**72.90**	**5.12**	**9.50**	**408.36**	**235.88**	**60.83**	**274.23**
Max	46.08	352.52	26.27	65.43	10117.97	246.88	106.86	1495.79	38.24	1273.45	827.67	30.16	58.11	735.78	423.63	115.60	522.85
Min	0.21	0.00	0.00	0.21	0.23	1.08	0.01	522.55	0.15	19.40	0.57	0.99	0.60	137.84	109.92	34.61	160.11
δ	7.71	37.12	2.94	11.49	929.47	26.51	18.81	166.82	7.72	239.70	134.33	4.35	7.46	95.82	65.09	13.64	60.65
Values	Sm	Eu	Gd	Tb	Dy	Ho	Er	Tm	Yb	Lu	Y	∑REY	Ce/Ce*	Eu/Eu*	La/Sm	La/Yb	Sm/Yb
Mean	**49.94**	**11.32**	**60.46**	**8.23**	**50.73**	**11.03**	**27.35**	**3.09**	**15.24**	**1.83**	**579.73**	**1798.25**	**0.31**	**0.93**	**1.22**	**16.43**	**14.06**
Max	94.59	19.97	110.98	15.33	91.10	18.83	44.72	4.86	22.17	2.79	900.46	3067.82	0.39	1.05	1.66	24.92	41.01
Min	28.61	6.12	35.04	4.76	30.53	6.32	13.41	1.31	5.16	0.53	282.18	969.24	0.27	0.83	0.47	12.25	9.96
δ	11.25	2.59	13.12	1.82	11.04	2.34	5.64	0.60	2.86	0.35	107.66	377.38	0.04	0.05	0.20	1.79	4.09

Note: δ Max means maximum value, Min means Minimum value. Data are calculated according to our previous studies (Yang et al., 2021; He et al., 2022; Yang et al., 2022).

4.3. Petrographic and chemical characteristics of collophanites

We previously reported the trace elemental compositions of collophanites, which included biodetritus and authigenic grains (Yang et al., 2021b; He et al., 2022; Yang et al., 2022), and the extreme values are listed in Table 3. The trace elements of all apatite aggregations were used to compare with apatite individuals. Overall, the apatite aggregations were enriched in Sr (mean of 1054.38 ppm), Ba (mean of 438.97 ppm), Zn (mean of 186.86 ppm), and REY (mean of 1798.25 ppm). Compare with apatite individuals, apatite aggregations have higher Cr, Sr, Ba, and Pb and lower V, Th, and U and contents (mean of 10.61 ppm, 1054.38 ppm, 438.97 ppm, 72.90 ppm, 4.32 ppm, 5.12 ppm, and 9.50 ppm, respectively) (Fig. 6). All apatite aggregations have MREE-rich REY patterns as characterized by weak enrichment of MREE relative to LREEs and HREEs (Fig. 7a). In addition, apatite aggregations have positive La, Gd, and Y anomalies, remarkably negative Ce anomalies, and Y/Ho ratios ranging from 44.65 to 57.69 (Table 3), in accordance with apatites with six-party apatite individuals (Table 1).

5. Discussion

5.1. Apatite individual types and origins

Previous studies suggested that sedimentary collophanite were homogeneous and uncrystallized. However, recent research showed that collophanite comprises closely-packed, nm–μm-scale apatites (Zhang et al., 2019; Liu and Zhou, 2020; Yang et al., 2021b), shown in Fig. 2 (g-i). Apatite individuals in Zhijin deposits have four different textures (Fig. 4). Among them, the six-party texture (Fig. 5a-c), consistent with apatite nano-crystals in collophanite, suggested they were both authigenic (discussed in Section 5.3). These cube-like textures belong to the hypidiomorphic texture (Fig. 5d-f), whereas granular and irregular belong to the allotriomorphic texture (Fig. 5g-i). This implied that they were rounded in seawater, carried over a longer distance, or underwent a certain degree of diagenesis. As we can see in Fig. 3, biodetritus, authigenic grains, and amorphous collophanite all contain apatite individuals. Even though apatite individuals were observed and researched, origins of the apatite individuals can not be identified only by the morphology as the texture of apatite has been destroyed during the mineral separation process. Nevertheless, in situ geochemistry, especially REY compositions, could provide further evidence.

Usually, sedimentary phosphorites show following four REY patterns: (a) shale-like/flat patterns characterized by small or absent Ce anomalies with little to no HREE enrichment; (b) MREE-enriched patterns with significantly negative Ce anomalies; (c) “bell-shaped” patterns with no Ce anomalies and depletion of LREE and HREE; and (d) seawater-like patterns characterized by negative Ce anomalies with varying degrees of HREE enrichment (McArthur and Walsh, 1984; Shields and Stille, 2001; Emsbo et al., 2015; Lumiste et al., 2021; Yang et al., 2022). Among them, MREE enrichment or bell-shaped patterns were widely recognized as secondary signatures rather than pristine seawater (Emsbo et al., 2015; Zhu and Jiang, 2017; Yang et al., 2022). Cerium anomalies in old phosphorites could be caused by diagenesis and only in partial cases recorded the redox conditions (Shields and Stille, 2001). Previous studies showed that both phosphorite bulk rocks and collophanites in Zhijin deposits have REY patterns with MREE-enriched and negative Ce anomalies (Zhang et al., 2003; Yang et al., 2021a; Zhang et al., 2021; He et al., 2022; Yang et al., 2022). In our study, type 1 apatite individuals have REY patterns similar to cotemporaneous collophanites (Fig. 8a, b), implying similar formation process. In addition, apatite individuals with bell- to flat- REY shapes were consistent with fossils, conodont, and phosphate sediments (Fig. 8c), consistent with diagenetic origin. Therefore, the apatite individuals from Zhijin phosphorites with MREE-enriched (type 1) and bell-shape to flat (type 4) REY patterns (Fig. 6a-c) potentially formed via precipitation and post-deposition. Combining the morphology (Fig. 5) and different

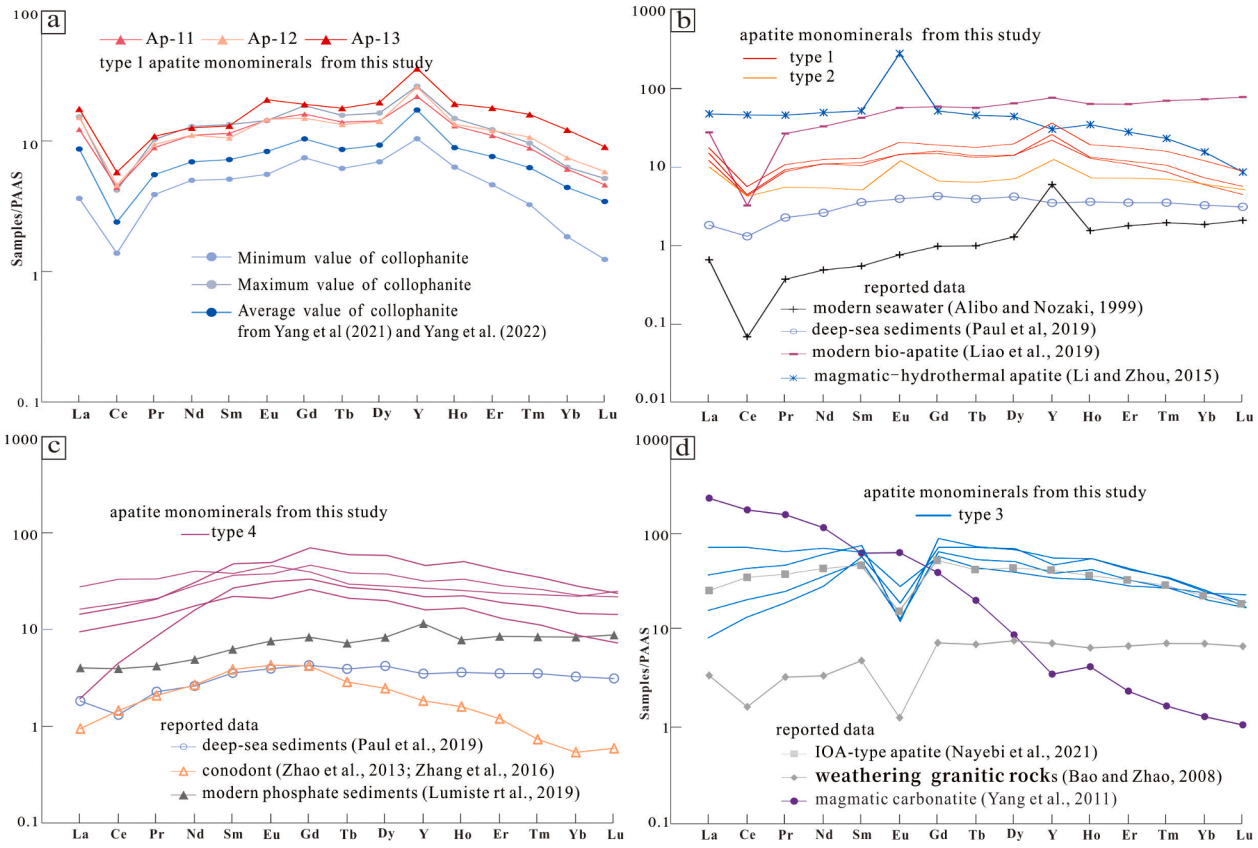

Fig. 8. Comparisons of PAAS-normalized REY distributions between apatite individuals and collophanite (a) and different geological objects (b, c, d). Apatite individuals are from this study, collophanites are from Yang et al. (2021b) and Yang et al. (2022); conodont came from Zhao et al. (2013); modern bio-apatite came from Liao et al. (2019); deep-sea sediments came from Paul et al. (2019); modern phosphate sediments came from Lumiste et al. (2019); modern seawater came from Alibo and Nozaki (1999); IOA-type apatite came from Nayebi et al. (2021); magmatic-hydrothermal apatites came from Li and Zhou (2015) and Xiao et al. (2021); weathering granitic rocks came from Bao and Zhao (2008), and magmatic carbonatite came from Yang et al. (2011).

Table 4a
Extreme values of rare earth element compositions of reported minerals, rocks, and seawater.

	values	Y	LREE	MREE	HREE	∑REE	∑REY	Y/Ho	Ce/Ce*	Eu/Eu*	La/Sm	La/Yb	Sm/Yb	Data sources
conodont	**Mean**	50.79	285.03	38.52	7.33	330.88	381.67	31.54	1.00	1.01	0.30	2.14	9.88	Zhao et al. (2013); Zhang et al. (2016)
	Max	451.60	2855.40	441.62	59.34	3216.09	3612.19	47.86	1.79	1.54	1.19	10.71	44.00	
	Min	1.20	5.24	0.60	0.19	6.03	7.23	11.11	0.62	0.67	0.00	0.06	1.24	
	δ	69.92	395.66	59.36	9.86	457.50	523.82	4.68	0.21	0.16	0.18	1.56	8.26	
modern bio-apatite	**Mean**	2094.71	2888.86	677.43	520.72	4087.01	6181.72	33.10	0.10	1.10	0.69	0.34	0.51	Liao et al. (2019)
	Max	6025.00	9358.00	2172.00	1310.70	12840.70	18865.70	40.00	0.20	1.29	0.89	0.69	1.05	
	Min	79.30	56.61	17.20	21.33	95.14	174.44	30.66	0.00	1.01	0.55	0.21	0.25	
	δ	1407.32	2266.46	505.57	310.68	3071.23	4469.62	1.59	0.05	0.04	0.08	0.10	0.18	
deep-sea sediments	**Mean**	96.49	304.98	46.92	26.26	378.16	474.64	26.15	0.72	1.00	0.52	0.57	1.10	Paul et al. (2019)
	Max	208.00	513.60	99.00	53.65	648.40	850.65	28.66	1.07	1.10	0.64	0.74	1.23	
	Min	51.70	181.00	24.80	14.33	223.16	275.16	24.64	0.27	0.95	0.44	0.48	0.96	
	δ	45.06	78.75	20.72	11.33	109.45	153.48	0.92	0.24	0.17	0.06	0.07	0.06	
modern phosphate sediments	**Mean**	317.75	712.48	91.61	64.33	868.42	1186.17	43.94	0.91	1.07	0.83	0.44	0.62	Lumiste et al. (2019)
	Max	990.00	2611.93	339.28	198.88	3147.39	4123.57	78.00	1.16	1.74	2.81	0.68	1.01	
	Min	10.67	9.78	2.66	2.02	14.77	25.44	33.12	0.56	0.63	0.54	0.19	0.10	
	δ	268.02	684.67	85.39	53.69	821.55	1083.57	9.23	0.15	0.17	0.45	0.10	0.24	
modern seawater	**Mean**	164.31	54.03	12.16	13.94	80.13	244.44	104.42	0.17	1.00	1.15	0.36	0.32	Alibo and Nozaki (1999)
	Max	252.20	103.07	20.94	22.77	146.78	398.98	114.29	0.43	1.11	1.39	0.41	0.44	
	Min	71.10	22.24	5.44	4.97	32.77	104.17	96.48	0.05	0.94	0.72	0.31	0.24	
	δ	63.59	22.68	4.80	6.34	33.70	97.01	3.75	0.12	0.04	0.20	0.02	0.06	

geological objects (Fig. 8), the apatite individuals (Ap-11, 12, 13) with authigenic textures and MREE-rich REY patterns agreed with those of collophanite (Fig. 8a), which indicated similar formation (discussed in Section 5.3). Among authigenic textures, apatite individuals with positive Eu anomalies reseble magmatic-hydrothermal apatites (Fig. 8b), indicating hydrothermal origins. Differently, apatite individuals having type 3 REY patterns (Ap-6 to Ap-9) and hypidiomorphic to allotriomorphic textures, were consistent with IOA-type apatites and weathering magmatic rocks (Frietsch and Perdahl, 1995; Bao and Zhao, 2008; Nayebi et al., 2021), which implied terrigenous origin (Fig. 8c).

Kon et al. (2104) proposed Ce and Eu-anomalies to distinguish REY origins in deep-sea mud in the Minami-Torishima area of Japan. Here,

Table 4b
Extreme values of rare earth element compositions of reported minerals, rocks, and seawater.

	values	Y	LREE	MREE	HREE	∑REE	∑REY	Y/Ho	Ce/Ce*	Eu/Eu*	La/Sm	La/Yb	Sm/Yb	Data sources
IOA-type apatite	**Mean**	1130.52	5749.90	491.14	213.95	6454.98	7585.51	30.91	1.08	0.31	0.44	1.15	2.35	Nayebi et al. (2021); Frietsch and Perdahl (1995)
	Max	11000.00	42230.00	2829.30	2085.70	43979.90	46059.90	35.63	1.24	0.51	1.09	5.95	6.83	
	Min	132.90	250.40	52.59	22.59	325.58	458.48	25.57	0.94	0.11	0.07	0.08	0.58	
	δ	1317.21	5640.59	417.18	257.55	6033.83	6784.18	1.70	0.06	0.09	0.30	0.99	0.92	
magmatic-hydrothermal apatites	**Mean**	1321.15	9548.65	850.54	256.98	10656.17	11977.32	25.16	0.95	2.80	0.63	2.21	2.99	Li and Zhou (2015); Xiao et al. (2021)
	Max	6500.00	29790.00	3325.00	1127.70	34242.70	40742.70	37.50	1.01	6.13	1.64	6.87	5.52	
	Min	9.44	60.80	44.42	0.91	164.11	209.09	13.67	0.83	1.18	0.07	0.09	0.34	
	δ	4299.06	9677.97	663.08	231.92	10248.46	10950.75	4.96	0.04	1.35	0.55	2.30	1.12	
weathering granitic rocks	**Mean**	201.94	433.06	77.67	53.83	564.56	766.50	30.70	0.65	0.25	0.66	1.01	1.12	Bao and Zhao (2008)
	Max	635.00	965.87	225.88	192.14	1131.38	1324.18	48.32	1.81	0.71	1.29	3.60	2.79	
	Min	27.95	48.25	10.54	8.60	114.57	142.52	24.69	0.20	0.02	0.10	0.02	0.20	
	δ	187.91	343.93	58.20	52.45	338.48	381.91	5.94	0.41	0.21	0.43	1.02	0.85	
magmatic carbonatite	**Mean**	96.99	28640.62	316.49	16.07	28973.18	29070.17	24.39	0.93	1.29	2.49	134.11	36.75	Yang et al. (2011)
	Max	506.00	192206.00	2612.00	70.96	194888.96	195394.96	47.50	1.01	1.79	8.98	552.96	96.88	
	Min	2.85	10.01	0.74	0.43	11.18	14.03	17.26	0.72	0.99	0.23	0.17	0.62	
	δ	126.32	51897.89	600.00	17.04	52478.38	52589.57	8.35	0.07	0.24	2.43	170.14	36.08	

Note: Initial rare earth elements in the references are normalized by PAAS (Taylor and McLennan, 1985) in this table. LREE = La + Ce + Pr + Nd + Sm; MREE = Eu + Gd + Tb + Dy; HREE = Ho + Er + Tm + Yb + Lu; $Ce^* = 2Ce_N/(La_N + Nd_N)$, $Eu/Eu^* = 2Eu_N/(Sm_N + Gd_N)$ (Bau and Dulski, 1996).

we recalculated Ce and Eu-anomalies of Zhijin collophanites and other reported geologic objects using PAAS normalization (Table 4). In the Ce vs Eu diagram (Fig. 9a), sediments, including conodont, modern phosphate sediments, and deep-sea mud, generally had Eu/Eu* ratios ~ 1.0 and variable Ce/Ce* ratios (~0.1–1.79) (Zhao et al., 2013; Zhang et al., 2016; Lumiste et al., 2019; Paul et al., 2019). Furthermore, modern seawater, as well as modern bio-apatite, has an Eu/Eu* ratio ~ 1.0 and lower Ce/Ce* (0.1–0.4) ratios (Alibo and Nozaki, 1999; Liao et al., 2019). However, iron-oxide-apatite (IOA)-type apatites and weathering magmatic rocks have lower Eu/Eu* ratios ~ 0.3 and variable Ce/Ce* ratios (~0.65–1.81) (Bao and Zhao, 2008; Nayebi et al., 2021). In addition, hydrothermal apatite has Eu/Eu* ratios ~ 1.0 and extremely high Eu/Eu* ratio of 6.13 (Li and Zhou, 2018; Xiao et al., 2021). In Ce/Ce* vs Eu/Eu* discrimination figures, Zhijin collophanites plotted in the seawater area (Fig. 9b), indicated the seawater autogenesis. The apatite individuals were plotted primarily in three areas: IOA-type ore, fossil apatite, and seawater (Fig. 9b). These were consistent with REY patterns (Fig. 8): apatites (Ap-11, 12, 13) with REY patterns similar to collophanite located close to collophanite; apatites having flat and bell-shaped REY patterns located at conodont and fossil area; apatites with REY patterns similar to IOA-type also located in the IOA ore area. In addition, Ap-10 had high positive Eu anomalies due to hydrothermal influences.

The REY patterns and Ce/Ce* vs Eu/Eu* figures suggested that the apatite individuals were divided into: authigenic apatites (AP-11, 12, and 13), diagenetic apatites (Ap-1 to Ap-5), terrigenous apatites (Ap-6 to Ap-9), and hydrothermally altered apatites (Ap-10). It implied that authigenic/diagenetic apatites might undergo authigenic formation and diagenetic alteration during deposition while other apatite individuals come from weathering of terrestrial volcanic rocks. Even though it is not quite distinguishable whether the biodetritus were mistaken for apatite individuals, slightly different REY compositions among these apatite individuals could be discussed to support the REY enrichment mechanism. Hence, apatite individuals could trace the sources of apatite and the REY, while authigenic/diagenetic apatites maintained formation and REY enrichment information of marine sedimentary apatites.

5.2. REY sources

Yttrium has a similar outer electron arrangement and radius with REEs (especially Ho), displaying highly coherent behavior. However, Y fractionates with REEs under certain conditions. The variation of Y with respect to Ho may provide additional geochemical information, such as to distinguish the sources (Bau and Dulski, 1995; Bau et al., 1995). In magmatic systems, neither partial melting nor fractional crystallization significantly fractionated Y from Ho, hence the apatites from magmatic systems had Y/Ho ratios close to chondrite (28) (Bau, 1996). Modern seawater have higher Y/Ho ratios ranging from 96 to 114 (Alibo and Nozaki, 1999). In addition, hydrothermal Y/Ho ratios have two groups of data, even though hydrothermal vein fluorites had variable Y/Ho ratios (up to 200), fluorites derived from and deposited near igneous rocks have Y/Ho ratios close to igneous source-rocks (Bau and Dulski, 1995), which was true in magmatic-hydrothermal apatites (~25) (Fig. 10) (Li and Zhou, 2015; Xiao et al., 2021). In the Y/Ho vs ∑REY figure (Fig. 10), authigenic apatites were located around collophanite and modern phosphate sediment areas (Yang et al., 2021b; He et al., 2022; Yang et al., 2022), while diagenetic apatites were close to bio-apatite and conodont (Zhao et al., 2013; Zhang et al., 2016; Liao et al., 2019) with lower Y/Ho and higher ∑REY. Terrestrial apatite individuals were located close to IOA-type apatites, magmatic and hydrothermal, and magmatic carbonite areas (Frietsch and Perdahl, 1995; Yang et al., 2011; Nayebi et al., 2021), while hydrothermal altered apatites located independently with lower ∑REY (Ap-10). These characteristics are consistent with REY PAAS-normalized patterns (Fig. 8) and Ce-Eu binary figure (Fig. 9), supporting the apatite classification. REY compositions and Y/Ho ratios of terrigenous clastic apatite individuals

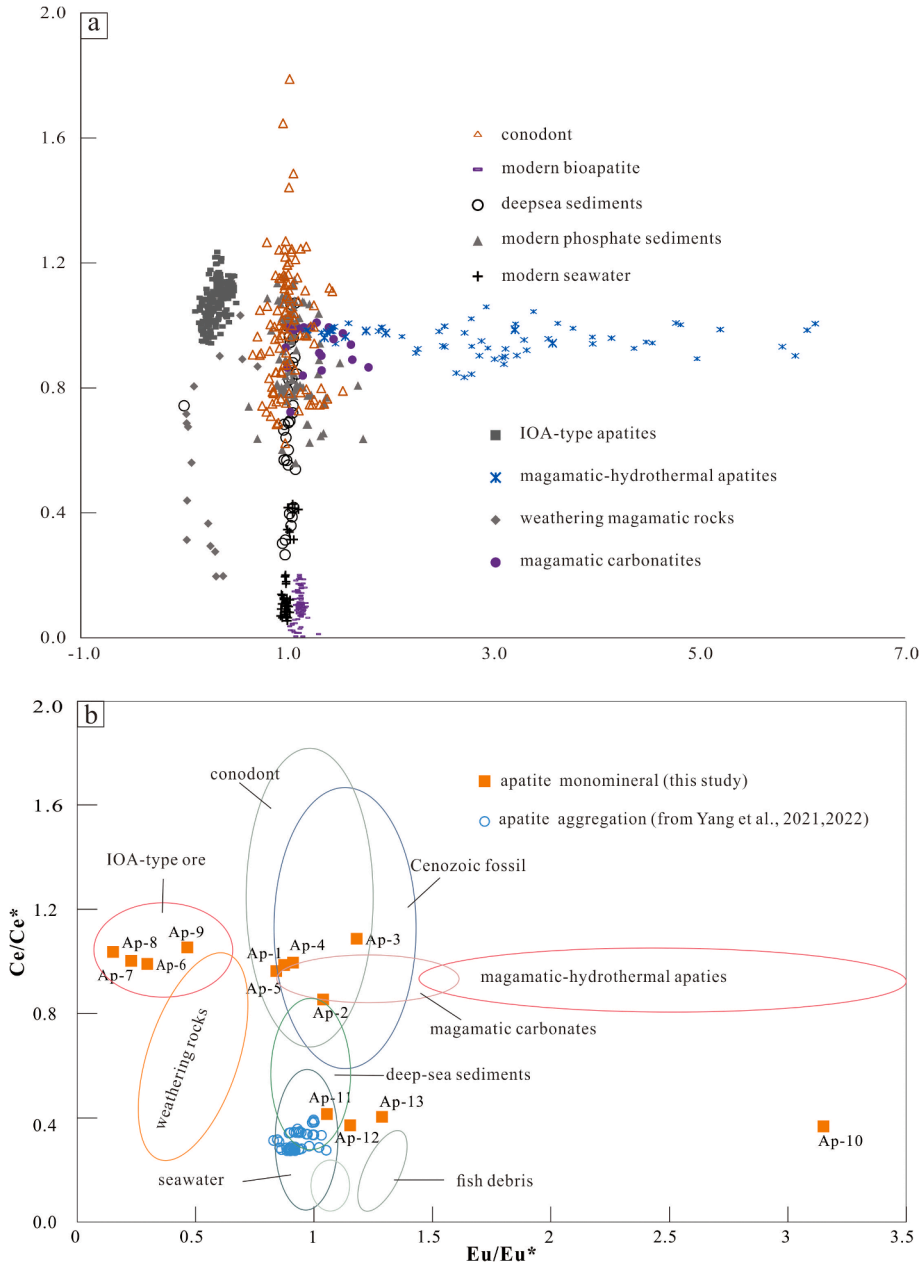

Fig. 9. Ce/Ce* and Eu/Eu* binary figure of different geologic objects (a) and Ce/Ce*-Eu/Eu* discriminant figure of the apatite sources (b). Base map and Ce/Ce* and Eu/Eu* according to Kon et al. (2104) and references therein, normalized by PAAS, data of different geological objects came same the same as data in Fig. 8.

indicated they came from terrestrial volcanic rock weathering and retained the initial Y/Ho ratios. However, authigenic/diagenetic apaties recoded the geochemistry of seawater during formation and diagenetic information.

The weathering of terrestrial volcanic rocks not only carried clastic apatite, but also provided high REY in seawater, as evidenced from Y/Ho vs REY of bulk phosphorite, collophanite, and apatite individuals. Previous studies showed that seawater had higher Y/Ho ratios, whereas terrestrial igneous rocks and weathering granites have lower Y/Ho (Alibo and Nozaki, 1999; Bao and Zhao, 2008; Yang et al., 2011). Hence the negative relationships between Y/Ho and ∑REY in phosphorite (Yang et al., 2021a) indicated that terrestrial inputs increased the ∑REY in seawater. This was consistent with apatite individuals, which usually have lower Y/Ho ratios and higher ∑REY (Fig. 9), especially for terrigenous apatites with high ∑REY levels between 4655 and 12232 ppm. Bau et al. (1995) reported that Y/Ho ratios ranged from 87 to 119 in South Pacific seawater at varying depths, consistent with data from the Boso Peninsula, Japan (96–114) (Alibo and Nozaki, 1999). The authigenic phosphorite rocks and collophanite have Y/Ho ratios between igneous rocks and seawater, which indicated an input mixture of terrestrial rocks and seawater and were consistent with previous studies (Yang et al., 2021a; He et al., 2022).

5.3. Formation of authigenic apatites

Previous studies reported REY in collophanites to reveal the apatite formation and REY enrichments. However, collophanites contain impurities including carbonates, quartz, organic matter, and other minerals (Fig. 2d-g) that inhibited the geochemical characteristics of phosphate minerals. Furthermore, the small diameters of apatite nanocrystals in collophanites limited a deeper understanding of the fine process of apatite formation and REY enrichment. Here, we analyzed the geochemistry of authigenic apatite individuals, compared to collophanites, to discuss the formation of authigenic apatites and REY

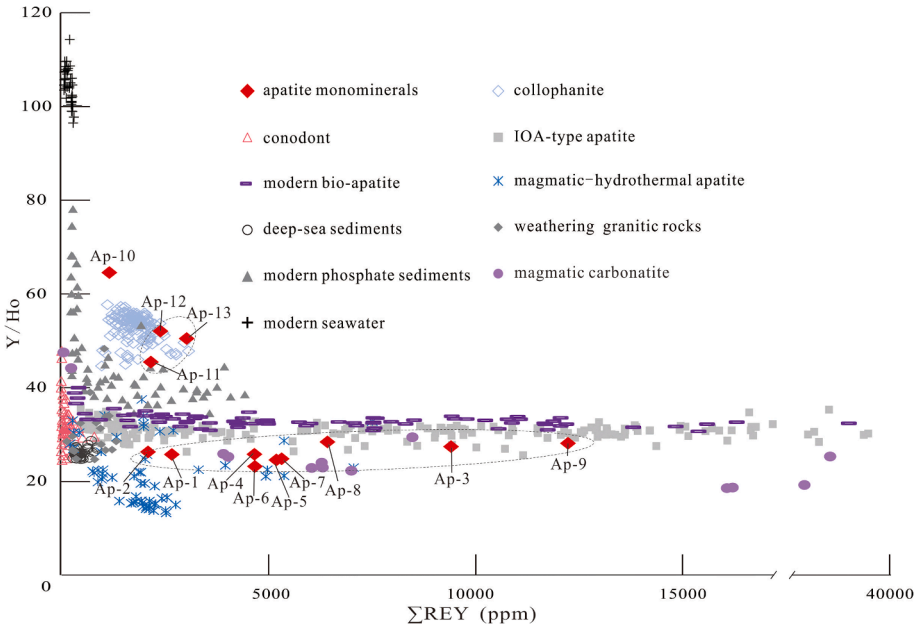

Fig. 10. Relationships between ∑REY and Y/Ho for different rocks, sediments, and seawater. Apatite individuals are from this study, collophanites came from Yang et al. (2021b) and Yang et al. (2022), and all reported data sources are the same as Fig. 8.

enrichment mechanisms. Apatite individuals were divided in four ways (Section 5.1), among them, authigenic/diagenetic apatites are used to discussed the formation mechanism and REY enrichment.

Previous studies showed that phosphogenesis went through prolonged diagenesis after precipitation (Shields and Stille, 2001; Chen et al., 2003), during which the phosphate mineral formed and the mineral phase transformed (Oxmann and Schwendenmann, 2014; Liao et al., 2019). Along with burial and diagenesis, CO_2 in apatites disappeared and high-carbon apatites transformed into low-carbon or carbon-free apatites (Liu, 1989). X-ray diffraction (XRD) showed that phosphate minerals in Zhijin deposits were carbon-free fluorapatite with small amounts of carbonate-fluorapatite, which indicated a diagenetic transformation (Liu, 2008; Yang et al., 2021b). Even though the content of selected individuals was not enough to analyze their XRD characteristics, authigenic apatite individuals have larger diameters (Figs. 3, 4, 5) than apatite nanocrystals in collophanites (Fig. 2h, i), resulting from that phosphate minerals transformed and grew up during diagenesis.

The geochemical characteristics of collophanites and apatite individuals were compared to discuss apatite formation, especially diagenesis (Shields and Stille, 2001; Lumiste et al., 2019; Lumiste et al., 2021; Yang et al., 2022). Lécuyer et al. (2004) proposed that a $(La/Sm)_N > 0.3$ represents initial conditions or slight alterations, while $(La/Sm)_N < 0.3$ come from the addition of REEs substituted into the crystals. Reynard et al. (1999) proposed a combined $(La/Yb)_N$ and $(La/Sm)_N$ plot to distinguish the diagenetic stage and mechanisms of REE incorporation in apatite. Previous reports showed that Zhijin collophanites have higher $(La/Yb)_N$ (2.0–3.2) and $(La/Sm)_N$ (>0.5), whereas authigenic apatite individuals have $(La/Sm)_N$ (1.1–1.4) and $(La/Yb)_N$ (1.4–2.1) similar to collophanite, which indicated early diagenetic adsorption instead of late substitution (Yang et al., 2021b; Zhang et al., 2021). However, diagenetic apatites have lower $(La/Sm)_N$ and $(La/Yb)_N$ ratios (0.07–0.73 and 0.13–1.25, respectively), which indicated they underwent stronger diagenesis than authigenic apatite. Other study showed that diagenesis caused REY redistribution and increased ∑REY and Ce levels (Shields and Stille, 2001). Authigenic apatite individuals had lower ∑REY, significantly negative Ce, and positive Y abnormalities relative to diagenetic apatites (Fig. 6a, c). This supported that diagenetic apatites enduring stronger diagenesis had higher REY and modified REY distributions, consistent with the Ce-Eu discriminant figure (Fig. 9b).

Meanwhile, Eu fractionated from other REY occurs via: (1) hydrothermal activities, (2) redox conditions, and (3) diagenetic modification. High temperatures (>250 °C), anoxic conditions, and diagenesis can increase Eu in apatites (Olivarez and Owen, 1991; Shields and Stille, 2001; Kidder et al., 2003; Deng et al., 2017). In Zhijin phosphorite, the Ce/Ce* ratios of collophanites (0.27–0.39) and apatite individuals (0.37–0.41) both indicated oxic conditions (Fig. 9), consistent with other isotopic indexes, such as Fe and Mo (Wen et al., 2010; Fan H.F. et al., 2016; Yang et al., 2021a). In addition, only noteworthy positive Eu anomalies were influenced by hydrothermal fluids, such as Ap-10. Hence, apatite individuals with weakly Eu/Eu* ratios indicated they underwent more remarkable diagenesis than collophanites during growth, rather than resulted from redox conditions (Fig. 9 b).

5.4. *REY enrichment mechanisms in authigenic apatites*

Ignoring the REY sources and secular variations of ∑REY in ocean chemistry, REY enrichment in Zhijin phosphorite could be controlled by the paleogeographic environment, Fe-redox pumping, biological absorption, and prolonged diagenesis (Kashiwabara et al., 2018; Yang et al., 2021b; Zhang et al., 2022). In this study, authigenic/diagenetic apatite individuals have much higher REY than collophanites (Fig. 8a), implying that there must be special factors caused apatite individuals to be enriched with REY. Firstly, formed in the same paleogeographic location, distinction between collophanites and authigenic apatite individuals could not be interpreted as paleogeographic environment. Secondly, in the definite case that early Cambrian seawater in South China was oxic (Wen et al., 2010; Fan H.F. et al., 2016; Yang et al., 2021a), organic matter or Fe/Mn oxides/hydroxides served as efficient traps for REY. Previous studies proposed that MREEs were preferentially adsorbed by organic matter or Fe/Mn oxides/hydroxides, then were released into pore water (Wright et al., 1987; Kidder and Eddydilek, 1994; Felitsyn and Morad, 2002). Thereafter, during diagenesis, REY was redistributed in pore water and the phosphate mineral phase, producing MREE-enrichment to bell-shaped patterns (Emsbo et al., 2015; Al-Bassam and Magna, 2018; Lumiste et al., 2021). These characteristics were found both in Zhijin collophanites and apatite individuals (Fig. 6), which indicated that preferential adsorption of MREEs and diagenetic modification controlled the REY enrichment. However, compared to

collophanites, apatite individuals in the Zhijin deposit were larger and had higher ∑REY; in addition, diagenetic apatite individuals had higher ∑REY (Tables 1, 3, Fig. 6). As discussed in Section 5.3, higher Eu/Eu* suggested more remarkable diagenesis of apatite individuals than apatite nanocrystals in collophanites. Hence, we conclude that during diagenesis, REY entered into apatite and enriched along with their growth.

6. Conclusions

(1) In early Cambrian Zhijin phosphorite deposits, REY-rich phosphate minerals developed mainly as collophanites, an aggregation of packed apatite nano-crystals and a small amount of apatite individuals. The apatite individuals have diameters between 40 and 100 μm and were divided into authigenic/diagenetic apatites, terrigenous clastic apatites, and hydrothermally altered apatites.

(2) In the South China ocean during the early Cambrian, weathering of terrestrial IOA deposits and magmatic-hydrothermal rocks carried clastic apatite and provided high REY into seawater. Furthermore, REY also came from deep seawater, resulting in mixed Y/Ho ratios in collophanites and authigenetic/diagenetic apatite individuals.

(3) Comparing the geochemical characteristics of collophanites, authigenic apatite individuals showed similar REY patterns, implying a similar formation process during which diagenetic modification played a vital role. Authegetic/diagenetic apatite individuals have larger diameters, higher Ce/Ce* and Eu/Eu* ratios, and lower $(La/Yb)_N$ and $(La/Sm)_N$ relative to collophanites, which suggested that apatite individuals underwent stronger diagenesis during formation.

(4) Preferential adsorption of MREEs and diagenetic modification might control REY enrichment in authigenic/diagenetic apatites, stronger diagenesis led to higher REY in larger apatite individuals. Organic matter or Fe/Mn oxides/hydroxides preferentially adsorbed REEs and subsequently released into pore water. During diagenesis, phosphate minerals transformed and grew, along with REY entering into apatite crystals.

Declaration of Competing Interest

The authors declare that they have no known competing financial interests or personal relationships that could have appeared to influence the work reported in this paper.

Data availability

Data will be made available on request.

Acknowledgements

The authors are grateful to Prof. Zhuojun Xie and Dr. Qinping Tan for their helpful suggestions toward improving the quality of this manuscript. This work was supported by the National Natural Science Foundation of China [Grant Numbers: 9206220039, 41872251, 41972095] and the Land and Resources Department of Yunnan Province [Grant Numbers: D202001, D201905].

The authors would like to thank all the reviewers who participated in the review and MJEditor (www.mjeditor.com) for its linguistic assistance during the preparation of this manuscript.

References

Al-Bassam, K., Magna, T., 2018. Distribution and significance of rare earth elements in Cenomanian-Turonian phosphate components and mudstones from the Bohemian Cretaceous Basin, Czech Republic. B. Geolsci. 93, 347–368.

Alibo, D.S., Nozaki, Y., 1999. Rare earth elements in seawater: Particle association, shale-normalization, and Ce oxidation. Geochim. Cosmochim. Acta 63, 363–372.

Bao, Z.W., Zhao, Z.H., 2008. Geochemistry of mineralization with exchangeable REY in the weathering crusts of granitic rocks in South China. Ore Geol. Rev. 33, 519–535.

Bau, M., 1996. Controls on the fractionation of isovalent trace elements in magmatic and aqueous systems: Evidence from Y/Ho, Zr/Hf, and lanthanide tetrad effect. Contrib. Mineral Petr. 123, 323–333.

Bau, M., Dulski, P., 1995. Comparative study of yttrium and rareearth element behaviours in fluorine-rich hydrothermal fluids. Contrib. Mineral Petr. 119, 213–223.

Bau, M., Dulski, P., 1996. Distribution of yttrium and rare-earth elements in the Penge and Kuruman iron-formations, Transvaal Supergroup, South Africa. Precambr. Res. 79, 37–55.

Bau, M., Dulski, P., Möller, P., 1995. Yttrium and holmium in South Pacific seawater: vertical distribution and possible fractionation mechanisms. Chem. Erde-Geochem. 55, 1–16.

Canfield, D.E., Poulton, S.W., Narbonne, G.M., 2007. Late-Neoproterozoic deep-ocean oxygenation and the rise of animal life. Science 315, 92–95.

Chen, D.F., Dong, W.Q., Qi, L., Chen, G.Q., Chen, X.P., 2003. Possible REE constraints on the depositional and diagenetic environment of Doushantuo Formation phosphorites containing the earliest metazoan fauna. Chem. Geol. 201, 103–118.

Chen, J.Y., Yang, R.D., Zhang, J., 2010. Mode of Occurrence of Rare Earth Elements in Posphorite in Zhijin County, Guizhou Province, China. Acta Mineralogica Sinica 30, 123–129 (in Chinese with English abstract).

Chen, J.Y., Yang, R.D., Wei, H.R., Gao, J.B., 2013. Rare earth element geochemistry of Cambrian phosphorites from the Yangtze Region. J. Rare Earth 31, 101–112.

Chew, D.M., Babechuk, M.G., Cogné, N., 2016. (LA, Q)-ICPMS trace-element analyses of Durango and McClure Mountain apatite and implications for making natural LA-ICPMS mineral standards. Chem. Geol. 435, 35–48.

Cook, P.J., 1992. Phosphogenesis around the Proterozoic Phanerozoic transition. J. Geol. Soc. 149, 615–620.

Cowie, J.W., Johnson, M.R.W., 1985. The chronology of the geological record. Geol. Soc. Lond. Mem.

Deng, Y.N., Ren, J.B., Guo, Q.J., Cao, J., Wang, H.F., Liu, C.H., 2017. Rare earth element geochemistry characteristics of seawater and porewater from deep sea in western Pacific. Sci. Rep-UK 7, article # https://doi.org/10.1038/s41598-41017-16379-41591.

Emsbo, P., McLaughlin, P.I., Breit, G.N., Bray, E.A.B., Koenig, A.E., 2015. Rare earth elements in sedimentary phosphate deposits: Solution to the global REE crisis? Gondwana Res. 27, 776–785.

Fan, H.F., Wen, H.J., Zhu, X.K., 2016a. Marine Redox Conditions in the Early Cambrian Ocean: Insights from the Lower Cambrian Phosphorite Deposits, South China. J. Earth Sci. 27, 282–296.

Fan, H.F., Wen, H.J., Xiao, C.Y., Zhou, T., Cloquet, C., Zhu, X.K., 2018. Zinc Geochemical Cycling in a Phosphorus-Rich Ocean During the Early Ediacaran. J. Geophys. Res. 123, 5248–5260.

Fan, H.R., Yang, K.F., Hu, F.F., Liu, S., Wang, K.Y., 2016b. The giant Bayan Obo REE-Nb-Fe deposit, China: Controversy and oregenesis. Geosci. Front. 7, 335–344.

Felitsyn, S., Morad, S., 2002. REE patterns in latest Neoproterozoic–early Cambrian phosphate concretions and associated organic matter. Chem. Geol. 187, 257–265.

Föllmi, K.B., Hosein, R., Arn, K.S., 2009. Weathering and the mobility of phosphorus in the catchments and forefields of the Rhone and Oberaar glaciers, central Switzerland: Implications for the global phosphorus cycle on glacial-interglacial timescales. Geochim. Cosmochim. Acta 73, 2252–2282.

Frei, R., Xu, L.G., Frederiksen, J.A., Lehmann, B., 2021. Signals of combined chromium-cadmium isotopes in basin waters of the Early Cambrian - Results from the Maoshi and Zhijin sections, Yangtze Platform, South China. Chem. Geol. 56 https://doi.org/10.1016/j.chemgeo.2021.120061.

Freslon, N., Bayon, G., Toucanne, S., Bermell, S., Bollinger, C., Cheron, S., Etoubleau, J., Germain, Y., Khripounoff, A., Ponzevera, E., Rouget, M.-L., 2014. Rare earth elements and neodymium isotopes in sedimentary organic matter. Geochim. Cosmochim. Acta 140, 177–198.

Frietsch, R., Perdahl, J.A., 1995. Rare earth elements in apatite and magnetite in Kiruna-type iron ores and some other iron ore types. Ore Geol. Rev. 9, 489–510.

He, S., Xia, Y., Xiao, J.F., Gregory, D., Xie, Z.J., Tan, Q.P., Yang, H.Y., Guo, H.Y., Wu, S. W., Gong, X.X., 2022. Geochemistry of REY-Enriched Phosphorites in Zhijin Region, Guizhou Province, SW China: Insight into the Origin of REY. Minerals 12. https://doi.org/10.3390/min12040408.

Henderson, P., 1984. Rare Earth Element Geochemistry. Elsevier Science Publishers, Amsterdam, p. 284.

Huang, Z.H., Qin, W.X., Hu, Y.M., Zhang, Y.S., 2021. Occurrence Characteristics of Rare Earth Elements in Typical Collophanite in Southwest China. Chinese J. Rare Metals 45, 695–701.

Jiang, S., Yang, J., Ling, H., Feng, H., Chen, Y., Chen, J., 2004. Re-Os isotopes and PGE geochemistry of black shales and intercalated Ni-Mo polymetallic sulfide bed from the Lower Cambrian Niutitang Formation, South China. Re-Os isotopes and PGE geochemistry of black shales and intercalated Ni-Mo polymetallic sulfide bed from the Lower Cambrian Niutitang Formation, South China 18–24.

Kashiwabara, T., Toda, R., Nakamura, K., Yasukawa, K., Fujinaga, K., Kubo, S., Nozaki, T., Takahashi, Y., Suzuki, K., Kato, Y., 2018. Synchrotron X-ray spectroscopic perspective on the formation mechanism of REY-rich muds in the Pacific Ocean. Synchrotron X-ray spectroscopic perspective on the formation mechanism of REY-rich muds in the Pacific Ocean 240, 274–292.

Kato, Y., Fujinaga, K., Nakamura, K., Takaya, Y., Kitamura, K., Ohta, J., Toda, R., Nakashima, T., Iwamori, H., 2011. Deep-sea mud in the Pacific Ocean as a potential resource for rare-earth elements. Nat. Geosci. 4, 535–539.

Kidder, D.L., Eddydilek, C.A., 1994. Rare-earth element variation in phosphate nodules from midcontinent Pennsylvanian cyclothems. J. Sediment. Res. 64, 584–592.

Kidder, D.L., Krishnaswamy, R., Mapes, R.H., 2003. Elemental mobility in phosphatic shales during concretion growth and implications for provenance analysis. Chem. Geol. 198, 335–353.
Kon, Y., Hoshino, M., Sanematsu, K., Morita, S., Tsunematsu, M., Okamoto, N., Yano, N., Tanaka, M., Takagi, T., 2104. Geochemical Characteristics of Apatite in Heavy REE-rich Deep-Sea Mud from Minami-Torishima Area, Southeastern Japan. Resour. Geol. 64, 47–57.
Lécuyer, C., Reynard, B., Grandjean, P., 2004. Rare earth element evolution of Phanerozoic seawater recorded in biogenic apatites. Chem. Geol. 204, 63–102.
Li, C.X., Zhou, M.F., 2015. Multiple stages of hydrothermal REE remobilization recorded in fluorapatite in the paleoproterozoic Yinachang Fe–Cu–(REE) deposit. Southwest China. Geochim. Cosmochim. Acta 166, 53–73.
Li, X.C., Zhou, M.F., 2018. The Nature and Origin of Hydrothermal REE Mineralization in the Sin Quyen Deposit, Northwestern Vietnam. Econ. Geol. 113, 645–673.
Liao, J.L., Sun, X.M., Li, D.F., Sa, R.N., Lu, Y., Lin, Z.Y., Xu, L., Zhan, R.Z., Pan, Y.G., Xu, H.F., 2019. New insights into nanostructure and geochemistry of bioapatite in REE-rich deep-sea sediments: LA-ICP-MS, TEM, and Z-contrast imaging studies. Chem. Geol. 512, 58–68.
Liu, S.R., 2008. Study of the Mineralization Process of Zhijin Xinhua Phosphate Deposit Using Microbeam Analyses. Chinese Academy of Sciences, p. 120. Chinese with English abstract).
Liu, Z.R.R., Zhou, M.F., 2020. Early Cambrian ocean mixing recorded by phosphorite successions in the Nanhua Basin, South China. Precambr. Res. 349, article # https://doi.org/10.1016/j.precamres.2019.105414.
Liu, X.Q., Zhang, H., Tang, Y., Long, L.Y., 2020. REE Geochemical Characteristic of Apatite: Implications for Ore Genesis of the Zhijin Phosphorite. Minerals 10, article # https://doi.org/10.3390/min10111012.
Liu, Y., Hou, Z.Q., Zhang, R.Q., Wang, P., Gao, J.F., Raschke, M.B., 2019. Zircon Alteration as a Proxy for Rare Earth Element Mineralization Processes in Carbonatite-Nordmarkite Complexes of the Mianning-Dechang Rare Earth Element Belt, China. Econ. Geol. 114, 719–744.
Liu, Y.S., Hu, Z.C., Gao, S., Günther, D., Xu, J., Gao, C.G., Chen, H.H., 2008. In situ analysis of major and trace elements of anhydrous minerals by LA-ICP-MS without applying an internal standard. Chem. Geol. 257, 34–43.
Liu, B.J., Xu, X.S., Xu, Q., Pan, X.N., Huang, H.Q., 1993. Sedimentary crustal evolution and mineralization of palaeocontinent in South China. Scientific Publications, Beijing, 236 pp (in Chinese).
Liu, Z.R.R., Zhou, M.F., 2017. Meishucun phosphorite succession (SW China) records redox changes of the early Cambrian ocean. Geol. Soc. Am. Bull. 129, 1554–1567.
Liu, K.W., 1989. The evolution of apatite inerals in the diagenetic processes. Acta Mineralogica Sinica 4, 310-323+385-386 (in Chinese with English abstract).
Lumiste, K., Lang, L., Paiste, P., Lepland, A., Kirsimäe, K., 2021. Heterogeneous REE + Y distribution in Early Paleozoic shelly phosphorites: Implications for enrichment mechanisms. Chem. Geol. 586, article # https://doi.org/10.1016/j.chemgeo.2021.120590.
Lumiste, K., Mänd, K., Bailey, J., Paiste, P., Lang, L., Lepland, A., Kirsimäe, K., 2019. REE +Y uptake and diagenesis in Recent sedimentary apatites. Chem. Geol. 525, 268–281.
McArthur, J.M., Walsh, J.N., 1984. Rare-earth geochemistry of phosphorites. Chem. Geol. 47, 191–220.
Nayebi, N., Esmaeily, D., Chew, D.M., Lehmann, B., Modabberi, S., 2021. Geochronological and geochemical evidence for multi-stage apatite in the Bafq iron metallogenic belt (Central Iran), with implications for the Chadormalu iron-apatite deposit. Ore Geol Rev 132.
Nelson, G.J., Pufahl, P.K., Hiatt, E.E., 2010. Paleoceanographic constraints on Precambrian phosphorite accumulation, Baraga Group, Michigan, USA. Sediment. Geol. 226, 9–21.
Olivarez, A.M., Owen, R.M., 1991. The europium anomaly of seawater: implications for fluvial versus hydrothermal REE inputs to the oceans. Chem. Geol. 92, 317–328.
Oxmann, J.F., Schwendenmann, L., 2014. Quantification of octacalcium phosphate, authigenic apatite and detrital apatite in coastal sediments using differential dissolution and standard addition. Ocean Sci. 10, 571–585.
Paul, S.A.L., Volz, J.B., Bau, M., Koster, M., Kasten, S., Koschinsky, A., 2019. Calcium phosphate control of REY patterns of siliceous-ooze-rich deep-sea sediments from the central equatorial Pacific. Geochim. Cosmochim. Acta 251, 56–72.
Planavsky, N.J., Rouxel, O.J., Bekker, A., Lalonde, S.V., Konhauser, K.O., Reinhard, C.T., Lyons, T.W., 2010. The evolution of the marine phosphate reservoir. Nature 467, 1088–1090.
Pufahl, P.K., Groat, L.A., 2017. Sedimentary and igneous phosphate deposits: formation and exploration: An invited Paper. Econ. Geol. 112, 483–516.
Reynard, B., Lécuyer, C., Grandjean, P., 1999. Crystal-chemical controls on rare-earth element concentrations in fossil biogenic apatites and implications for paleoenvironmental reconstructions. Chem. Geol. 155, 233–241.
Shi, C.H., 2005. Formation of phosphorite deposit, Breakup of Rodinia supercontinent and Biology explosion- A case study of Weng'an, Kaiyang and Zhijin phosphorite deposits of Guizhou Province. University of Chinese Academy of Sciences, p. 108 (Ph. D. thesis) (in Chinese with English abstract).
Shields, G., Stille, P., 2001. Diagenetic constraints on the use of cerium anomalies as palaeoseawater redox proxies: an isotopic and REE study of Cambrian phosphorites. Chem. Geol. 175, 29–48.
Shu, L.S., 2012. An analysis of principal features of tectonic evolution in South China Block. Geol. Bull. China 31, 1035–1053 (in Chinese with English abstract).
Steiner, M., Wallis, E., Ertman, B.D., Zhao, Y.L., Yang, R.D., 2001. Submarine hydrothermal exhalative ore layers in black shales from South China and associated fossils insights into Lower Cambrian facies and bio-evolution. Paleogeogr. Palaeocl. 169, 165–169.
Taylor, S.R., McLennan, S.M., 1985. The Continental Crust: Its Composition and Evolution, An Examination of the Geochemical Record Preserved in Sedimentary Rocks. Blackwell Scientific Publications, Oxford, p. 312.
Wang, J., Li, Z.X., 2003. History of Neoproterozoic rift basins in South China: implications for Rodinia break-up. Precambr. Res. 122, 141–158.
Wang, D.H., Zhao, Z., Yu, Y., Dai, J.J., Deng, M.C., Zhao, T., Liu, L.J., 2018. Exploration and research progress on ion-adsorption type REE deposit in South China. China Geol. 1, 415–424.
Wen, H.J., Zhang, Y.X., Fan, H.F., Hu, R.Z., 2010. Mo isotopes in the Lower Cambrian formation of southern China and its implications on paleo-ocean environment. Chin. Sci. Bull. 54, 4756–4762 (in Chinese with English abstract).
Wright, J., Schrader, H., Holser, W.T., 1987. Paleoredox variations in ancient oceans recorded by rare earth elements in fossil apatite. Geochim. Cosmochim. Acta 51, 631–644.
Wu, X.H., Han, Z.J., Cai, J.F., 1999. Guizhou phosphorite. Geological Publishing House, Beijing, 339 pp (in Chinese with English abstract).
Xiao, B., Pan, Y.M., Song, H., Song, W.L., Zhang, Y., Chen, H.Y., 2021. Hydrothermal alteration processes of fluorapatite and implications for REE remobilization and mineralization. Contrib. Mineral. Petr. 176 https://doi.org/10.1007/s00410-00021-01849-00417.
Xu, L.G., Lehmann, B., Mao, J.W., Qu, W.J., Du, A.D., 2011. Re-Os age of polymetallic Ni-Mo-PGE-Au mineralization in early Cambrian black shales of South China - a reassessment. Econ. Geol. 106, 511–522.
Yang, K.F., Fan, H.R., Santosh, M., Hu, F.F., Wang, K.Y., 2011. Mesoproterozoic carbonatitic magmatism in the Bayan Obo deposit, Inner Mongolia, North China: Constraints for the mechanism of super accumulation of rare earth elements. Ore Geol. Rev. 40, 122–131.
Yang, J.D., Sun, W.G., Wang, Z.Z., Wang, Y.X., 1996. Sm-Nd isotopic age of Precambrian Cambrian boundary in China. Sm-Nd isotopic age of Precambrian Cambrian boundary in China 133, 53–61.
Yang, H.Y., Xiao, J.F., Xia, Y., Xie, Z.J., Tan, Q.P., Xu, J.B., He, S., Wu, S.W., Liu, X.Q., Gong, X.X., 2021a. Phosphorite generative processes around the Precambrian-Cambrian boundary in South China: An integrated study of Mo and phosphate O isotopic compositions. Geosci. Front. 12, 1–27.
Yang, H.Y., Zhao, Z.F., Xia, Y., Xiao, J.F., 2021b. REY enrichment mechanisms in the early Cambrian phosphorite from South China. Sediment. Geol. 426 https://doi.org/10.1016/j.sedgeo.2021.106041.
Yang, H.Y., Xiao, J.F., Xia, Y., Zhao, Z.F., Xie, Z.J., He, S., Wu, S.W., 2022. Diagenesis of Ediacaran – early Cambrian phosphorite: Comparisons with recent phosphate sediments based on LA-ICP-MS and EMPA. Ore Geol. Rev. 144 https://doi.org/10.1016/j.oregeorev.2022.104813.
Ye, L.J., Chen, Q.Y., Liu, K.W., 1989. Chinese phosphorite rock. Science Press, Beijing, 339 pp (in Chinese).
Ye, X.T., Zhu, W.G., Zhong, H., He, D.F., Ren, T., Bai, Z.J., Fan, H.P., Hu, W.J., 2013. Zircon U-Pb and chalcopyrite Re-Os geochronology, REE geochemistry of the Yinachang Fe-Cu-REE deposit in Yunnan Province and its geological significance. Acta Petrologica Sinica 29, 1167–1186.
Yuan, Z.X., Li, J.K., Wang, D.H., Zhen, G.D., Lou, D.B., Chen, Z.H., Zhao, Z., Yu, Y., 2012. Metallogenic regularity of rare earth deposits in China. Geological Publishing House (Beijing), Beijin, p. 117.
Zhang, L., Algeo, T.J., Cao, L., Zhao, L., Chen, Z.-Q., Li, Z., 2016. Diagenetic uptake of rare earth elements by conodont apatite. Paleogeogr. Palaeocl. 458, 176–197.
Zhang, H., Fan, H., Wen, H., Han, T., Zhou, T., Xia, Y., 2022. Controls of REY enrichment in the early Cambrian phosphorites. Geochim. Cosmochim. Acta 324, 117–139.
Zhang, Y.B., Gong, M.L., Li, H., 2007. Occurrence of REE in Rare Earth Phosphorite in Zhijin Area, Guizhou. J. Earth Sci. Enviro. 29, 362–368 (in Chinese with English abstract).
Zhang, Z.Y., Jiang, Y.H., Niu, H.C., Xing, J.Q., Yan, S., Li, A., Weng, Q., Zhao, X.C., 2021. Enrichment of rare earth elements in the early Cambrian Zhijin phosphorite deposit, SW China: Evidence from francolite micro-petrography and geochemistry. Ore Geol. Rev. 138 https://doi.org/10.1016/j.oregeorev.2021.104342 article #.
Zhang, G.W., Li, S.Z., Dong, Y.P., Liu, S.F., He, D.F., Cheng, S.Y., Lu, R.K., Yao, A.P., 2013. Structure and the problems of the South China continent. Chin. Sci. Bull. 3, 1553–1582 (in Chinese with English abstract).
Zhang, Y.G., Pufahl, P.K., Du, Y.S., Chen, G.Y., Liu, J.Z., Chen, Q.G., Wang, Z.P., Yu, W. C., 2019. Economic phosphorite from the Ediacaran Doushantuo Formation, South China, and the Neoproterozoic-Cambrian Phosphogenic Event. Sediment. Geol. 388, 1–19.
Zhang, J., Zhang, Q., Chen, D.L., 2003. REE geochemistry of the Ore-bearing REE in Xinhua phosphorite, Zhijin, Guizhou. J. Mineral. Petrol. 23, 35–38 (in Chinese with English abstract).
Zhao, L.S., Chen, Z.Q., Algeo, T.J., Chen, J., Chen, Y., Tong, J., Gao, S., Zhou, L., Hu, Z., Liu, Y., Jiedong, 2013. Rare-earth element patterns in conodont albid crowns: evidence for massive inputs of volcanic ash during the latest Permian biocrisis? Global. Planet. Change 105, 135–151.
Zhu, B., Jiang, S.Y., 2017. LA-ICP-MS analysis of rare earth elements on phosphatic grains of the Ediacaran Doushantuo phosphorite at Weng'an, South China: implication for depositional conditions and diagenetic processes. Geol. Mag. 154, 1381–1397.